SPECTRAL DECOMPOSITION AND INVERSION: CASE STUDY OF A PRODUCTION AREA IN THE COOK INLET BASIN, ALASKA, USA

A Thesis

Presented to

the Faculty of the Department of Earth

and Atmospheric Sciences

University of Houston

In Partial Fulfillment

of the Requirements for the Degree

Master of Science

By

Jesus M. Rodriguez

May, 2009

SPECTRAL DECOMPOSITION AND INVERSION:

CASE STUDY OF A PRODUCTION AREA IN

THE COOK INLET BASIN, ALASKA, USA

Jesus M. Rodriguez

APPROVED:

Dr. John P. Castagna, Chairman

Dr. Janok Bhattacharya

Dr. Henry Posamentier

Dean College of Natural Sciences and Mathematics

ACKNOWLEDGEMENTS

My special thanks go to Dr. John Castagna for his advice, encouragement, and the confidence and support he has given me throughout this effort. My sincerest gratitude to my committee members Dr.Bhattacharya and Dr. Posamentier for their helpful contributions and suggestions.

I want to thank the Fusion's family, in particular Carlos Moreno, Alan Huffman, Maria Perez, Freddy Obregon, and Carlos Cobos; I appreciate your support and thank you for the many technical lessons. I would also like to thank Marathon Oil Company. I appreciate all the help I received from Bruce Shang, Don Caldwell, Gail Liebelt, Courtney McElmoyl, Mark Petersen, and a special thanks to Mark Quakenbush for his efforts, encouragement, and support.

I want to thank the entire Geosciences department at University of Houston and recognize the help from my friends Charles, Rafael, Tai, Felipe, Jeremy, Alejandro, Maria, Chirag, and Jadranka.

To Alejandro Morelos and his family: you made me feel welcomed and appreciated when I arrived in Houston and made me part of your family. Thanks for your advices and support.

I want to thank my family, especially my Mom, Dad, and my brothers Francisco and Antolin. You have been always my role models.

Finally, I must be grateful of having my beautiful wife, the love of my life at my side every day and every second. Thanks Raquel for your love, encouragement, patience, and loyalty. This goal is from both of us and I devoted it to you. I love you.

SPECTRAL DECOMPOSITION AND INVERSION: CASE STUDY OF A PRODUCTION AREA IN THE COOK INLET BASIN, ALASKA, USA

An Abstract of a Thesis

Presented to

the Faculty of the Department of Earth

and Atmospheric Sciences

University of Houston

In Partial Fulfillment

of the Requirements for the Degree

Master of Science

By

Jesus M. Rodriguez

May, 2009

ABSTRACT

Two or more seismic events, closely spaced compared to the dominant wavelength of the seismic wavelet, produce interference effects that can limit the theoretical resolution limit. Spectral decomposition and spectral inversion are processes that can improve seismic images by allowing the identification of stratal continuity and resolving layer thicknesses that could not be seen otherwise. In the absence of noise, synthetic wedge models have suggested that the classical $\lambda/8$ limit of seismic resolution does not limit the resolution of the inversion outcome. Spectral decomposition and inversion techniques were applied to a seismic dataset from Alaska, resulting in a considerably improved vertical resolution, which helped in identifying and delineating thin gas sands that were below tuning. The attributes also provided geomorphologic information, allowing interpretation and visualization of a braided depositional system on the Sterling Formation that corresponds with the regional geology and an analog from the Sagavanirktok River, Alaska.

CONTENTS

LIST OF FIGURES

1. INTRODUCTION

1.1 Characterization Needs of Thin Reservoirs

In subsurface exploration and production, the goal is not to focus only on determining the geological framework, reservoir structural configuration, and rock and fluid properties, but also to recognize the internal stratigraphy, lateral continuity, and connectivity of sedimentary bodies. Of these parameters, the most difficult to determine are the ones below vertical resolution, particularly for seismically thin layers. Vertical seismic resolution is defined as the ability to separate or distinguish between two or more close events (reflections) in the time/depth domain (Chopra et al., 2006). Widess (1973) defines the resolution limit as $1/8^{th}$ of the wavelength ($\lambda/8$). The tuning thickness (Kallweit and Wood, 1982) usually occurs at about $\lambda/4$, and in practice, beds below tuning are not readily resolved. This thesis focuses on development and application of novel processing techniques that improve vertical resolution in seismic data.

The theory of spectral decomposition offers the possibility of imaging geologic features below seismic resolution, for thickness determination (Partyka, et al., 1999), reservoir delineation, and stratigraphic visualization (Marfurt and Kirlin, 2001). The concept behind spectral decomposition is that for a given time, the spectrum of a trace can be represented and explained as the superposition or sum of the wavelet spectra (Castagna, et al., 2003). Recent studies (Burnett et al., 2003; Castagna et al., 2003; Hernandez and Castagna, 2004; Fahmy et al., 2005; Sinha et al., 2005; Odebeatu et al.,

2006; Rauch-Davies and Graham, 2006) have shown that spectral decomposition (SD) can also be used as a direct hydrocarbon indicator, as the presence of hydrocarbon produces specific effects that can be revealed in the frequency domain.

Spectral inversion combines the principles of spectral decomposition and seismic inversion to extend the theoretical resolution limit below $\lambda/8$, where the seismic amplitude and frequency response is more sensitive to thin beds (Castagna, 2005; Portniaguine and Castagna, 2005; Chopra, et al., 2006; Puryear and Castagna, 2008). Going beyond the seismic resolution limit will help the geoscientist to produce a more detailed and quantitative interpretation.

1.2 The Problem

Spectral decomposition and spectral inversion techniques were applied to several synthetic wedge models (forward modeling) to show the potential impact of the methods on seismic interpretation. The methods were then applied to a 3D seismic dataset from a production area of the Cook Inlet Basin, located in the Matanuska Valley along the Alaskan peninsula.

2. THEORY

2.1 Constructive and Destructive Interference

The theoretical limit of vertical resolution is $1/8^{th}$ of the wavelength ($\lambda/8$) (Widess, 1973), which is half the tuning thickness (Kallweit and Wood, 1982). The tuning thickness is related to constructive and destructive interference between reflections (Figure 1). However, this limit ($\lambda/8$) is compromised in the presence of noise; therefore geophysicists usually assume $\lambda/4$ as the resolution limit.

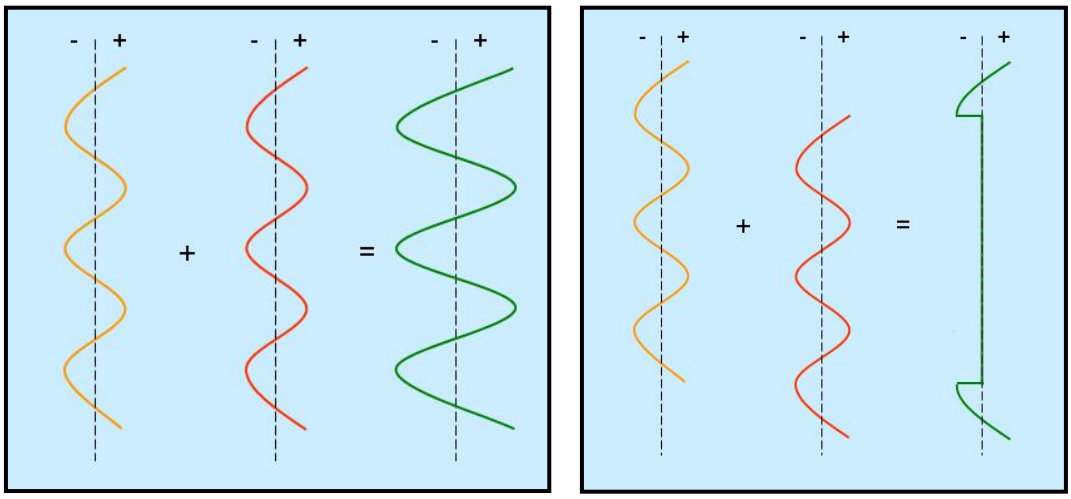

Figure 1: Definition of constructive (left) and destructive (right) interference. Constructive means both top and bottom reflections have the same sign at certain depths, while destructive means they have the opposite sign. Therefore, two closely-spaced seismic events as compared to the dominant wavelength of the seismic wavelet produce interference effects that can limit the theoretical resolution limit.

The signal/noise ratio (S/N) is highly variable and dependent on acquisition parameters, subsurface geologic complexity (structural and stratigraphic), and fluid and rock properties. Therefore, the limit of resolution is affected by the presence of noise and other factors, such as rock age, depth, velocity, and dominant frequency. The relationship between velocity and frequency defines the wavelength of the seismic data and its theoretical resolution limits.

A synthetic wedge model was created from a pair of opposite reflection coefficients, and was convolved with a Ricker wavelet of 25 Hz (Figure 2), where the average velocity is 3400 m/s. The model shows that below $\lambda/4$, both events start destructively interfering (34 m thickness), whereas at $\lambda/8$ the dimming in amplitude due to this interference is more evident (17m thickness). This would be considered the resolution limit for this synthetic example with high S/N ratio. Visually however, it is evident that below 1/4 wavelength, top and base reflectors cannot be mapped independently.

Assuming that the average seismic data spectrum lies between 15-35 Hz, a shallow young reservoir, with a frequency spectrum around 35 Hz, and a velocity of approximately 3500 m/s (see Brown, 1999), would show a wavelength close to 100m. Given $\lambda/4$ or $\lambda/8$ (high S/N data) as the resolution limit (Widess, 1973), any layer less than 25 or 12.5 meters thick respectively, might not be resolved by seismic reflections (top and base) below $\lambda/4$, as is shown in the synthetic example (Figure 2). Because many

reservoir layers are < 20 m thick, they cannot be resolved with conventional seismic processing, thus a new technique is needed to improve resolution.

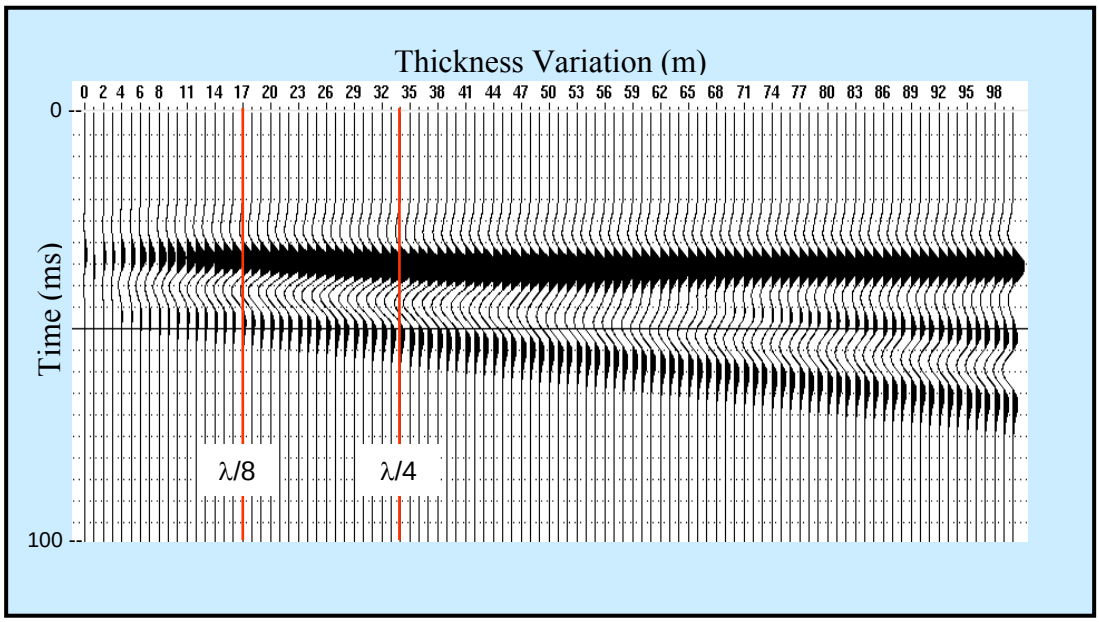

Figure 2: Synthetic wedge model convolved with a 25 Hz Ricker wavelet, shows the theoretical resolution limits λ/4 and λ/8 (red), beyond λ/4, the top and base reflectors interfere with each other, because the thickness is less and the convolved wavelet cannot resolve it.

2.2 The Spectral Decomposition (SD) Concept

Spectral decomposition (SD) is the representation or analysis of a seismic trace using the frequency domain via the Fourier transform (Figure 3). A time-frequency analysis resulting from spectral decomposition is the superposition of the wavelet spectra occurring (Figure 3) as a function of time (Castagna, et al., 2003).

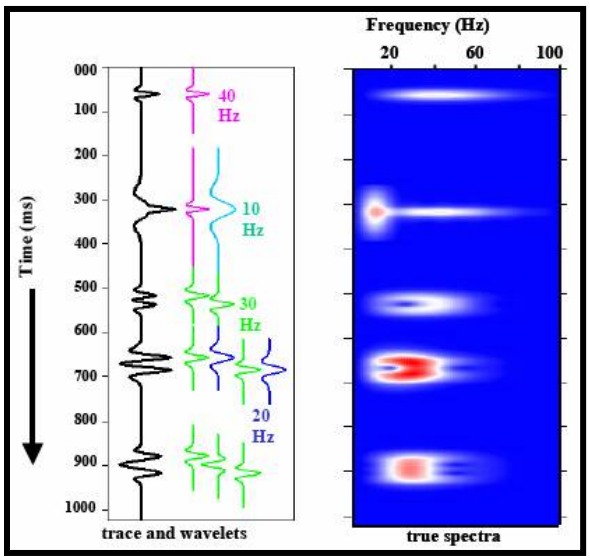

Figure 3: Spectral decomposition concept shown on a frequency gather. For a given time, the spectrum of a seismogram is the superposition of the wavelet spectra (from Castagna et al., 2003).

Partyka et al. (1999) show that the expression of a thin bed seismic reflection in the frequency domain is indicative of its temporal thickness (Figure 4). By knowing the wavelet of a source and looking at its spectrum, a thin bed model can be illustrated and compared with the wavelet (Figure 4). The spectrum of that thin bed will look similar to the wavelet in frequency content, except that it will show notches corresponding to the

local rock mass variability, shown as different modal distributions. These modal distributions, also called notches, are important, since there is an inverse relationship between the periodicity of the notches (Figure 4) and the temporal thickness (Gridley and Partyka, 1997). The discrete Fourier transform (DFT) allows imaging and mapping of temporal bed thickness and geologic discontinuities over large 3-D seismic surveys (Partyka et al., 1999).

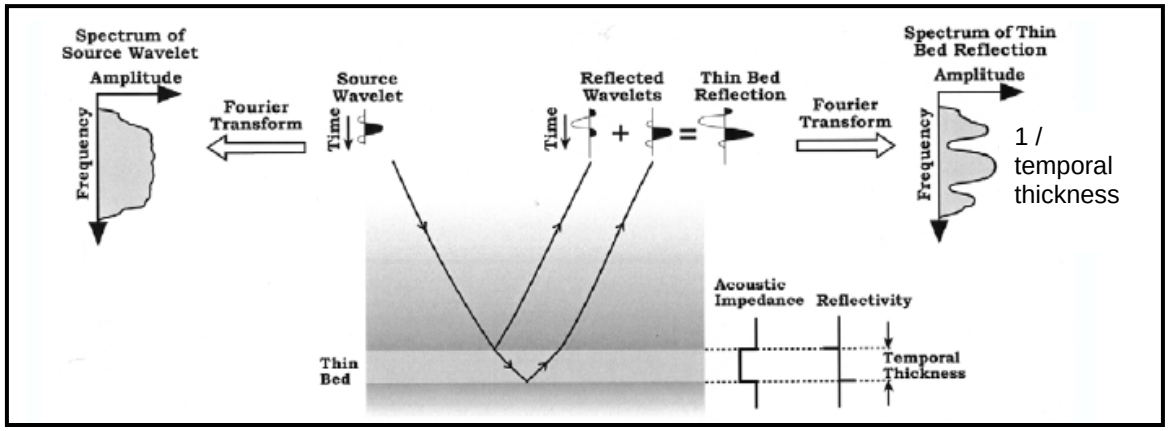

Figure 4: Thin bed model and spectral imaging (from Partyka et al., 1999).

How is this frequency domain seen in seismic data? Figure 3 shows the example for a single trace, but for a 2D seismic section two axes represent the time and CDP variation and of course the amplitude component is contained in the traces. This 2D line is transformed to the frequency domain, where a 3D cube will be created from it. The same line will have a different amplitude representation at each frequency (Figure 5), implying that if all the frequency sections are summed, the result will be the original 2D seismic line.

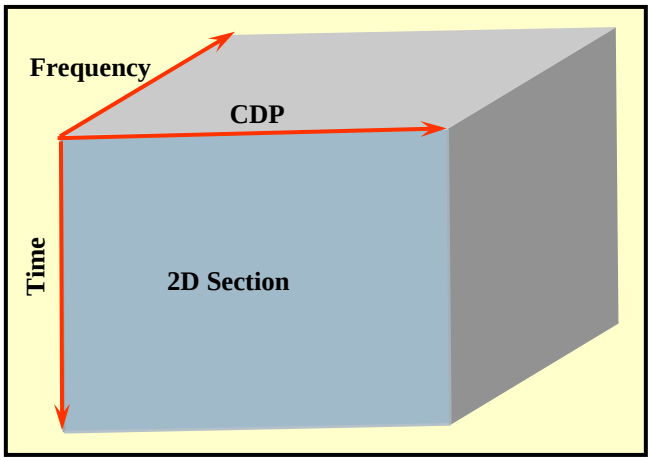

Figure 5: Representation of the frequency domain on a 2D line. The sum of all the amplitude sections at each frequency will result in the original amplitude section.

The response of a long window seismic trace, which is the result of the reflectivity series convolved with a wavelet plus some noise, can be compared and observed in the frequency domain (figure 6). The wavelet acts like a filter suppressing higher and lower frequencies. The seismic trace spectrum's shape is similar to the wavelet spectrum plus the noise.

On the other hand, a short window frequency analysis of the same seismic trace shows that the geology also acts like a filter. For that reason, the seismic trace will contain the spectrum of the reflectivity series (layer thickness) inside the limits of the wavelet spectra (Figure 7). It is important to compare the difference between these two spectrums (short and long window). The response from a short window is more related to the acoustic properties and thicknesses of the beds, whereas the long window analysis better describes the background.

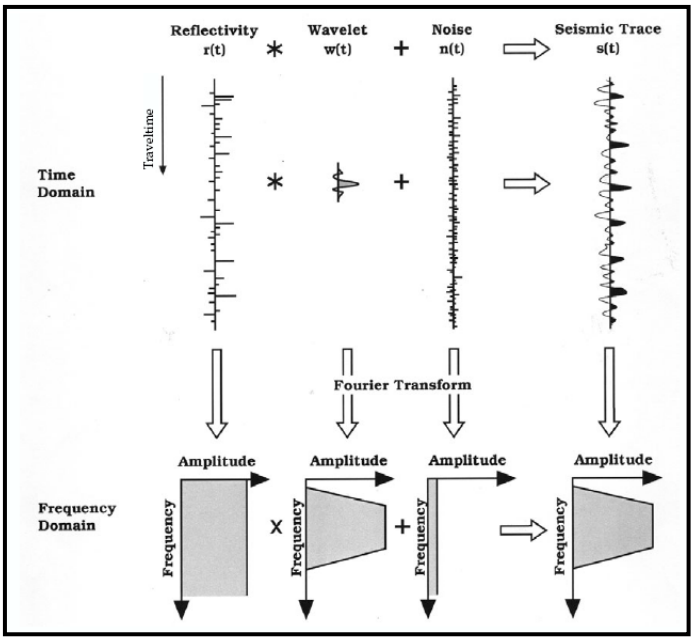

Figure 6: Long time window SD showing a flat (white) amplitude spectrum in the frequency domain. When the trace is convolved with a wavelet, the spectrum of the trace is overprinted by the wavelet spectrum, acting as a filter. The resulting seismic trace will look similar to the wavelet plus the noise spectrum (from Partyka et al., 1999).

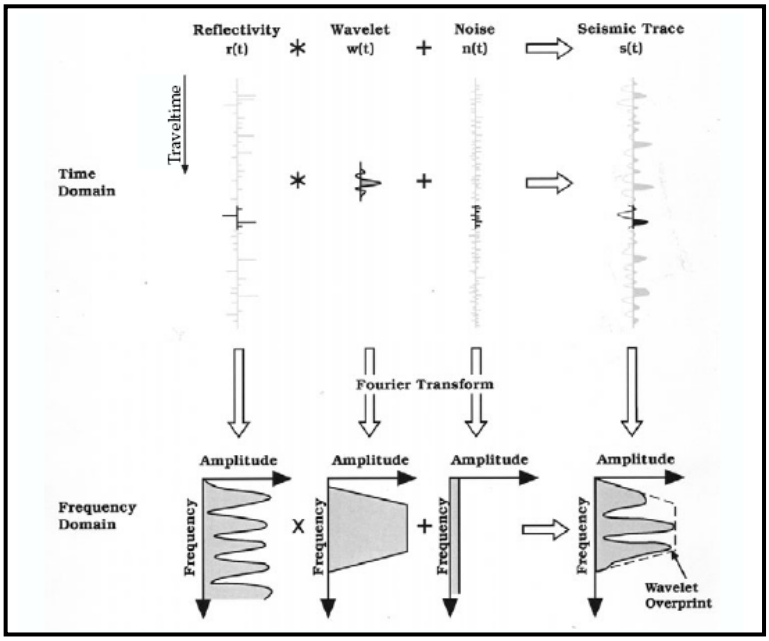

Figure 7: Short time window spectral decomposition showing that the response is dependent on the thickness and acoustic properties of the layers within the window. The amplitude spectrum of the resulting seismic trace will be the spectrum of the short window reflectivity overprinted by the wavelet, the local layering properties will be preserved within the spectrum (from Partyka et al., 1999).

2.3 Spectral Decomposition Methods

Different techniques have been created and utilized for SD. Some of them have been described and analyzed before by Chakraborty and Okaya (1995), Castagna et al. (2003), and Castagna and Sun (2006). All methods have advantages and disadvantages, because the same problem can be solved by different methods. The spectral decomposition process is not a unique process, as is the case with any seismic inversion. The key is to use the method that will approach the desired solution faster, capturing the essential features important for interpretation.

Castagna et al. (2003) suggest some conditions that should be met to determine when a spectral decomposition algorithm is useful or not. These requirements are: 1) the vertical resolution should be very similar to the seismogram; 2) the stack of the frequency gather (sum of the amplitudes over frequencies) should be equivalent to the instantaneous amplitude of the seismic trace; 3) the sum of all frequency spectra over time should approximate the spectrum of the seismic trace; 4) side lobes should not appear as events in the frequency domain; 5) the amplitude spectrum of an isolated event should not be distorted or smeared, and 6) spectral notches should not be related to time separation of resolvable events.

Traditionally, the methods most often utilized are those based on the Fourier transform (FT), like the fast Fourier transform (FFT) and discrete Fourier transform (DFT) (Partyka et al., 1999). FFT and DFT methods require the use of a time window,

producing a distortion of the true spectra and vertical resolution of the output (Figure 8). The FT methods show that the window is an important factor, either for the vertical resolution or the spectral resolution. Hence, a long window is better to use to determine the frequency content of the data, but it will mix different vertical events (Figure 8a). On the other hand, a short window shows better vertical resolution but the spectral resolution is smeared (Figures 8b). Thus, FT methods fail in conditions (4-6) noted above.

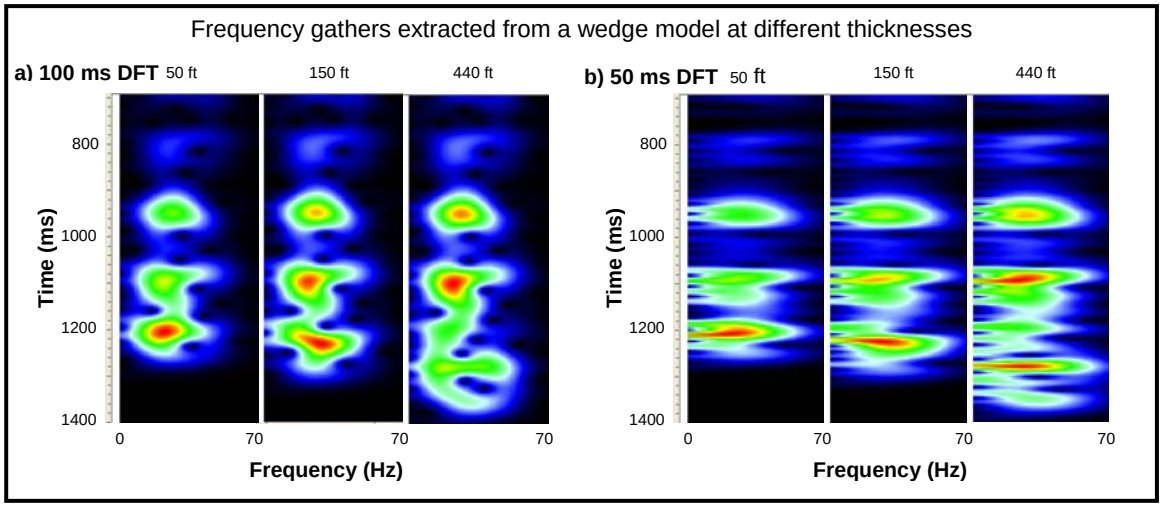

Figure 8: Comparison of a**:** a) long time window DFT (100ms) and b) short time window DFT (50 ms); frequency gathers extracted from a synthetic wedge model, each gather represents different thickness (50, 150 and 440 ft). The top of the wedge is located at 1200 ms. When the window is smaller the vertical resolution is improved but the spectral resolution is smeared.

The continuous Wavelet Transform (CWT) has some advantages over the DFT for broad-band signals. It is equivalent to temporal narrow-band filtering of the seismic trace but the disadvantage is that an orthogonal wavelet dictionary is required (Castagna and Sun, 2006). Figure 9a shows that CWT has good time resolution for high frequencies and good frequency resolution for lower frequencies. Therefore, the problem turns out to

be in the middle frequencies. What happens with all the intermediate frequencies? How can we improve this considering that most seismic data is typically band limited between 10 to 70 Hz (Chakraborty and Okaya, 1995)?

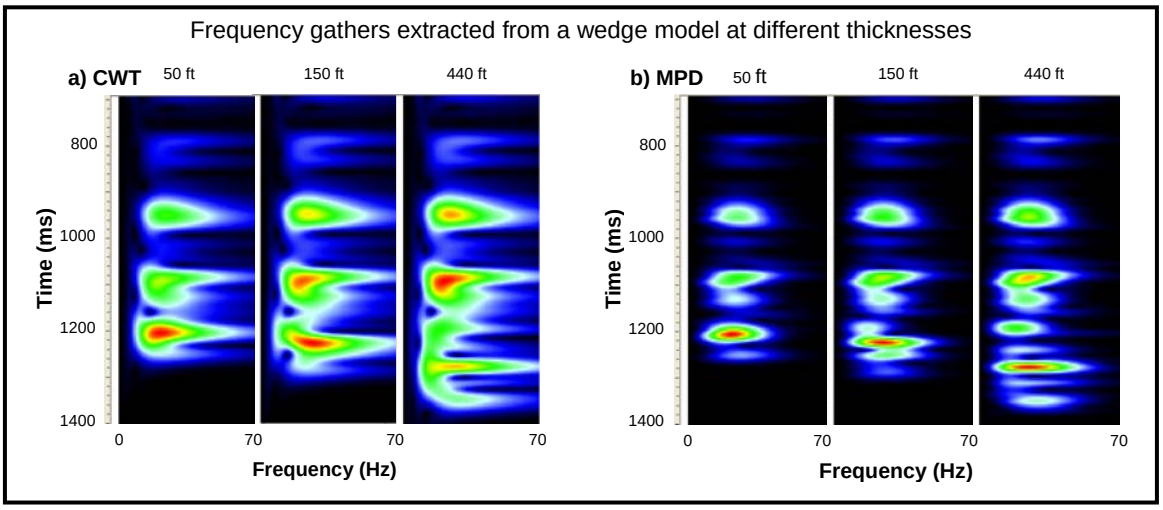

Figure 9: Comparison of frequency gathers extracted from a synthetic wedge model, each gather represents different thickness (50, 150 and 440 ft respectively). The top of the wedge is located at 1200 ms. CWT (a) analysis improves the spectral resolution at lower frequencies compared with DFT, but MPD (b) analysis improves both the vertical and spectral resolution significantly.

Mallat and Zhang (1993) developed a method meeting the conditions 1 through 6 called Matching Pursuit Decomposition (MPD). MPD involves cross-correlation of the seismic trace against a wavelet dictionary. The projection of the best correlating wavelet on the seismic trace is then subtracted from that trace. The wavelet dictionary is then cross-correlated against the residual, and the best projection is subtracted again. This process will be repeated iteratively until the residual falls below an acceptable threshold. The wavelets need not be orthogonal, and there is no windowing or corresponding spectral smearing (Castagna and Sun, 2006). Figure 9b (right) shows the results from

MPD where the time and spectral resolution are remarkably better than other methods, meeting the conditions described before by Castagna et al. (2003). For these reasons MPD and derivatives are the most powerful methods of spectral decomposition (Castagna et al, 2003; Castagna and Sun, 2006).

2.4 Spectral Decomposition Application as a DHI Tool

Recent reservoir studies, where spectral decomposition was applied either to predict or confirm the presence of hydrocarbons, have shown that the presence of hydrocarbon accumulations on seismic data produces some effects that can be exposed by SD (Burnett et al., 2003; Castagna et al. 2003; Ebrom, 2004; Hernandez and Castagna, 2004; Fahmy et al., 2005; Sinha et al., 2005; Castagna and Sun, 2006; Odebeatu et al., 2006; Rauch-Davies et al., 2006).

Castagna et al. (2003) mentioned four effects or ways in which SD can help in the direct detection of hydrocarbons, 1) abnormally high attenuation, 2) low-frequency shadows, 3) tuning frequency anomalies (also called differential reservoir reflectivity or preferential reservoir illumination), and 4) frequency-dependent AVO.

Low-frequency shadows (Figure 10) beneath amplitude anomalies (reservoirs) where the thickness is not sufficient to result in significant attenuation, have been used as a hydrocarbon indicator. In exploration, these shadows are often attributed to high

attenuation in gas reservoirs (Castagna et al., 2003), but finding a unique explanation to the occurrence of low-frequency reflections underneath gas or condensate reservoirs is not easy. Ebrom (2004) discusses 10 possible mechanisms for low-frequency shadows and how they could be related to the presence of hydrocarbons. Ebrom (2004) states that, even though the detection of anomalous zones is clearly the first step in applying this possible direct hydrocarbon indicator, it would still be of use to determine the cause of the effect. Castagna et al. (2003) state that low-frequency zones beneath reservoirs may not necessarily be caused by attenuation, and it is often difficult to explain observed shadows under thin reservoirs where there are insufficient travel paths through the absorbing gas reservoir to justify the observed shift of spectral energy from high to low frequencies.

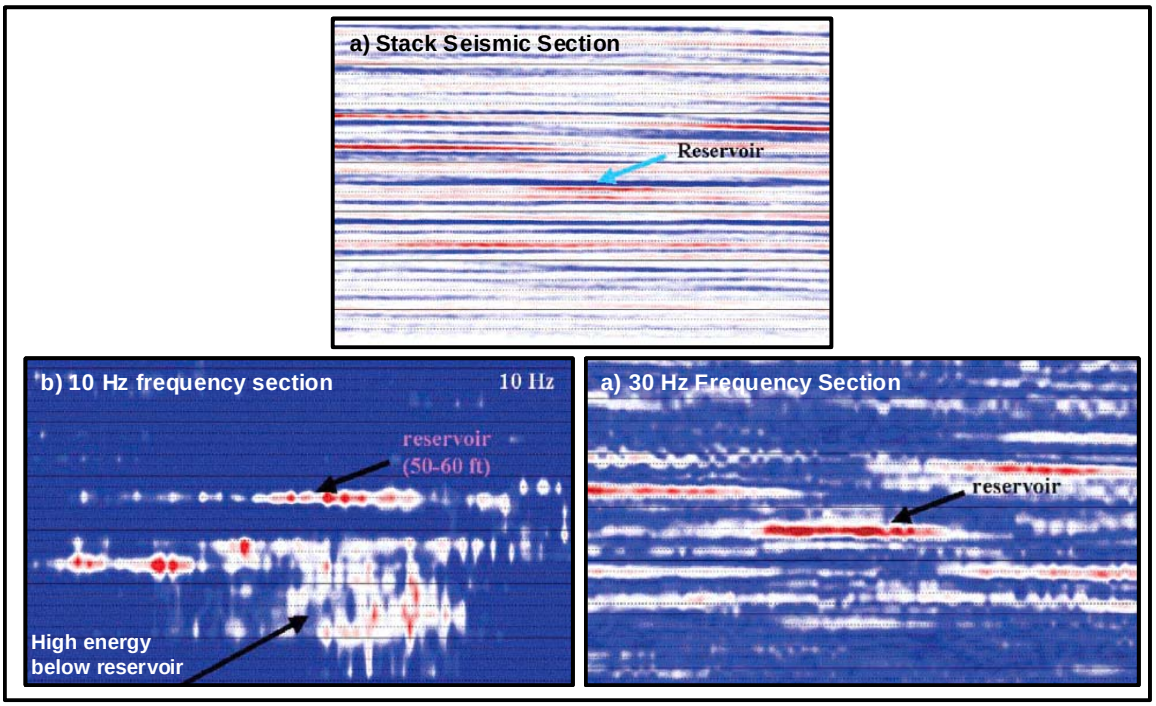

Figure 10: a) Broad-band migrated stack seismic section. Troughs are blue and peaks red. The reservoir is a classic bright spot. b) 10 Hz common frequency section; significant high energy occurs below reservoir. c) 30 Hz common frequency section, the low frequency shadow disappears. Time lines are 20 ms (from Castagna et al., 2003).

2.5 Spectral Inversion

2.5.1 Spectral Inversion Concept

Contrary to Widess' conclusions, recent studies (Tirado, 2004; Portniaguine and Castagna, 2005; Castagna, 2005; Chopra, et al., 2006; Puryear and Castagna, 2008) explain how the theoretical resolution limit extends farther than λ/8, where the seismic amplitude and frequency response is more sensitive to "thin beds", where the reflections from top and base of a layer exhibit maximum constructive interference at a layer thickness of λ/4. Below this point, the waveform and peak frequency continue changing while amplitude decreases until λ/8, where the waveform approximates the time derivative of the seismic wavelet and the amplitude decreases (Figure 2 and 11). Beyond λ/8 the amplitude response approaches zero for zero thickness and the waveform does not change considerably (Chopra, et al., 2006; Puryear and Castagna, 2008).

A synthetic wedge model example, with an amplitude vs. thickness plot representation for both top and base reflections, shows that the amplitude finds its maximum at λ/4 (tuning) and then gradually decreases almost linearly with thickness due to destructive interference (Figure 11). However, the shape of the waveform is preserved below λ/8. Notice that both events, top and base, decrease symmetrically; whereas above λ/4 the amplitude values and constructive interference decrease until corresponding to the real reflectivity series.

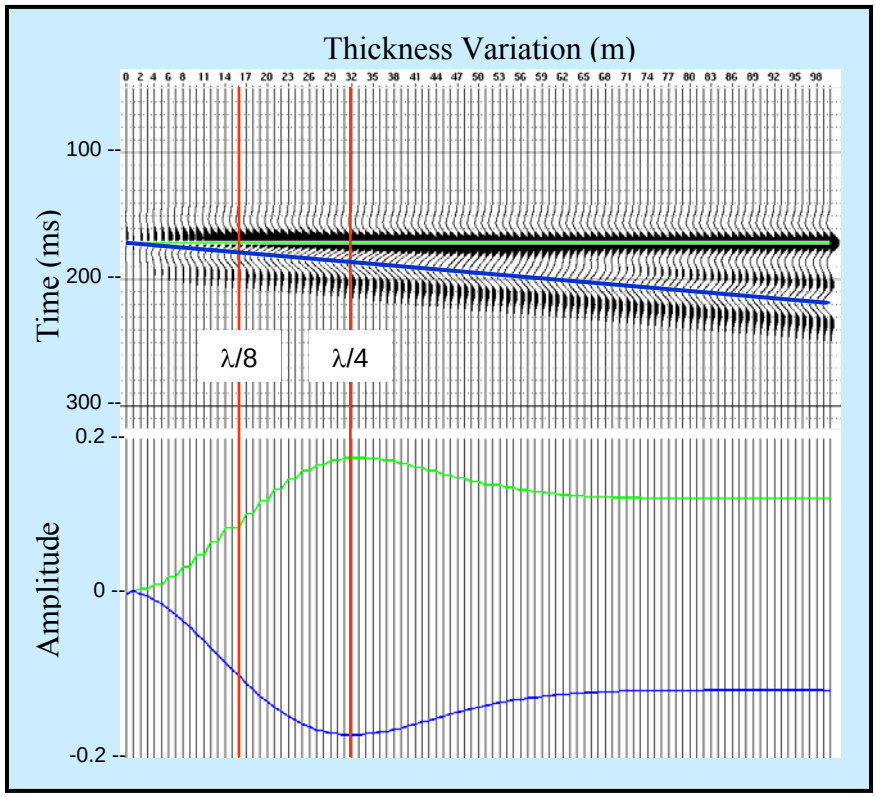

Figure 11: A synthetic wedge model convolved with a 25 Hz Ricker wavelet (above) and a plot of amplitude vs thickness (below) show the amplitude variation with thickness at the top and base of the wedge. The 100 traces represent thickness variation.

Applying the concept of SD, it is possible to go beyond the λ/8 limit, resulting in a more detailed and quantitative interpretation. The theory of the spectral inversion method relies more on the geology than in mathematical assumptions (Chopra et. al., 2006) and the use of spectral decomposition. Consider a pair of reflection coefficients that represent a thin bed. Any pair of reflection coefficients can be described as the sum of the other two (Figure 12), where one reflection coefficient pair has the same polarity and magnitudes, called the even component, whereas the other one has the same magnitude but opposite polarity, called the odd component (Castagna, 2005; Chopra et al., 2006).

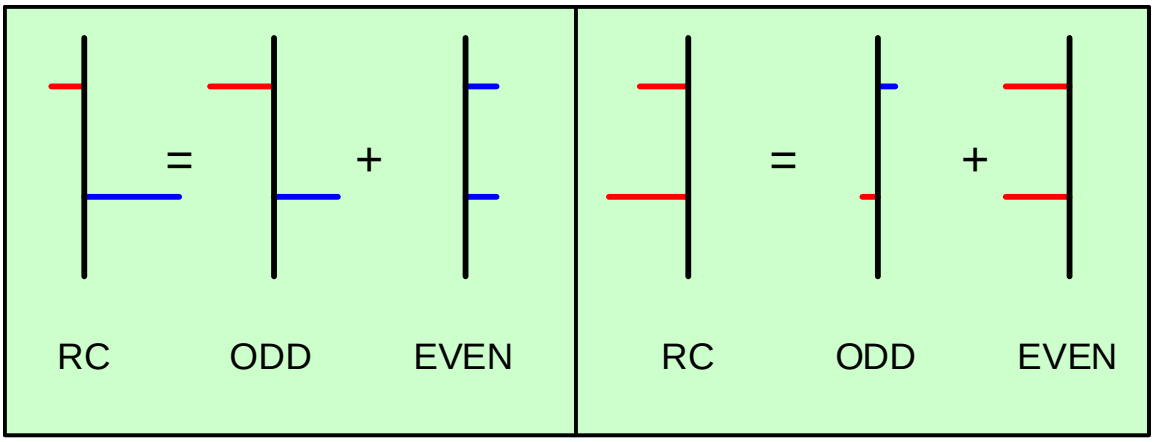

Figure 12: Two examples of a pair of arbitrary reflection coefficients representing thin beds. Any pair of reflection coefficients can be represented as the sum of an odd and even component. The odd component has opposite polarity and the same magnitude, whereas the even component has the same polarity and magnitude.

The maximum amplitude (peak amplitude) vs. thickness analysis for each of these components (odd and even) shows that the odd part finds its maximum amplitude at tuning and then decreases as the thickness also goes to zero. In contrast, the even component becomes more important below approximately half of tuning and behaves just the opposite (Figure 13). The even component is closer to the real value of the reflection due to constructive interference, and the odd component cancels itself and goes to zero (destructive interference). From the peak-amplitude analysis (Figure 13) it can be concluded that the even component significantly contributes to the improvement in vertical resolution, guiding the reflection coefficient result toward the real data value. Above $\lambda/8$, both components contribute up to a point (close to $\lambda/4$), where the odd component adds more to the solution, and the even provides less. The odd component behaves approximately as the Widess model suggests, resolving thick beds above $\lambda/4$, whereas the even component guides the solution for thin beds.

The peak-frequency analysis vs. thickness (instant-frequency value associated at every peak amplitude) shows that the odd component continues increasing, while thickness is reduced to around half tuning (a dipole effect). Similarly, the even component also continues increasing, with thickness reduction contributing more to the total solution. The total peak frequency gradually increases, as thickness decreases, but below a certain thickness (close to λ/8), the peak frequency changes and decreases to the same peak frequency of the wavelet instead of the derivative of the wavelet (Chopra et. al., 2006, Puryear and Castagna, 2008). This suggests the seismic data response is more sensitive to thin seismic beds than previously thought (Chopra et. al., 2006).

Accordingly, the amplitude and frequency components vary beyond the theoretical limit of seismic resolution. The approach based on spectral decomposition potentially allows thicknesses below the resolution limit of the bandwidth to be recovered.

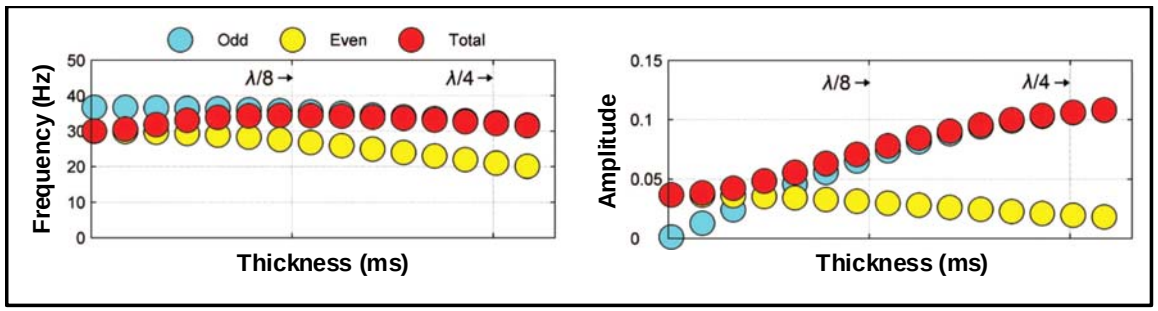

Figure 13: Peak frequency (left) and peak amplitude (right) as a function of time thickness for the even and odd components, as well as the total. There is peak amplitude and frequency information below the tuning thickness. The total peak amplitude comes close to the even component amplitude (from Puryear and Castagna, 2008).

2.5.2 Single-Layer Case

Portniaguine and Castagna (2005) discuss an inversion method using post-stack data that can resolve thin layers, where the operation is applied trace by trace. On every seismic trace, the fingerprint of the contained wavelet is removed by inverting via the spectral decomposition concept. However, this method needs to consider two steps. It is necessary to estimate a set of wavelets that varies in time and space; this is why well control is advantageous. If no well control is available, a statistical method to determine the wavelet has to be applied (Chopra et al., 2006). The second step is to remove the wavelets (filter) from the data with a seismic inversion process, using the concept of SD. This inversion method does not rely on an initial model; it has no horizons or lateral continuity constraints. It is not essential to have well data constraint, although well data provides useful control points and help verify the quality of the results (Chopra et al., 2006).

Puryear and Castagna (2008) discuss the theory of spectral inversion and developed an algorithm to invert reflectivity. This algorithm is based on the constant periodicity (peaks and notches) produced by layer thicknesses in the frequency domain (Figure 14) as previously stated by Partyka et al. (1999) and Marfurt and Kirlin (2001).

The algorithm described by Puryear and Castagna (2008) was developed by applying Fourier transforms in time windows to various reflectivity models and analyzing the amplitude spectrum for a layer of a given thickness. The space (periodicity) between

the notches and/or peaks is inversely related to the layer's time thickness (Figure 14) (Partyka et al., 1999; Marfurt and Kirlin, 2001). Therefore, with a narrow band frequency and high S/N dataset, the layer thickness can then be predicted, if the band is broad enough to resolve the periodicity (Puryear and Castagna, 2008).

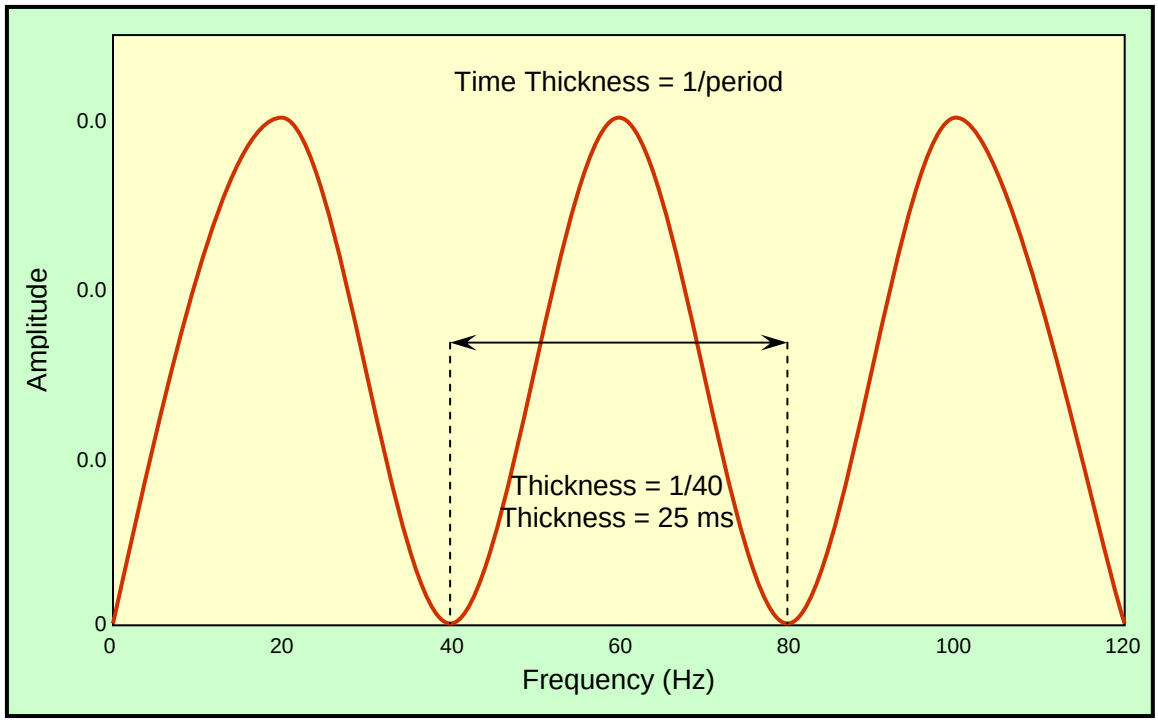

Figure 14: Amplitude vs Frequency plot for a thin layer thickness of 25 ms. Temporal thickness is 1/period which is equal to 1/40**.**

Marfurt and Kirlin (2001) defined an expression for a two layer reflectivity model:

$$g(t) = r_1\delta(t - t_1) + r_2\delta(t - t_1 - T) \quad (1)$$

where r_1 and r_2 are the top and base reflection coefficients respectively, t is a time sample, t_1 is the time sample at the top reflection and T is the layer thickness based on Figure 15.

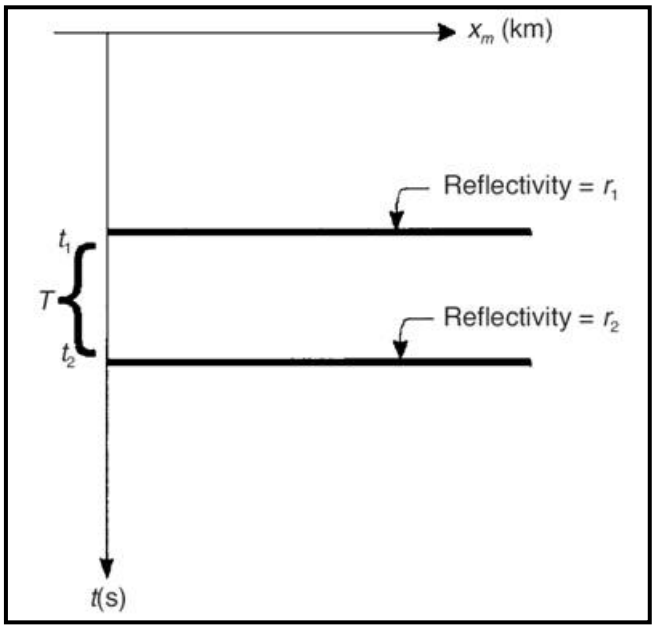

Figure 15: A two layer reflectivity model (from Marfurt and Kirlin, 2001).

Puryear and Castagna (2008) modified equation 1 by defining T relative to the center of the layer. The Fourier transform is applied and trigonometric identities used for simplification, and the real and imaginary parts are obtained. The real part (*Re*) is:

$$\mathrm{Re}[g(f)] = (2r_e)\cos(\pi\ f\ T) \tag{2}$$

where f is frequency, $g(f)$ is the complex spectrum, and r_e is the even component of the reflection coefficient pair.

Correspondingly, the imaginary part (*Im*) is:

$$\mathrm{Im}[g(f)] = (2r_o)\sin(\pi\ f\ T) \tag{3}$$

where r_o is the odd component of the reflection coefficient pair.

The constant period in the spectrum is related to the symmetrical point in the center of the layer for each real and imaginary component. The precise position splits the reflection coefficient pair perfectly into an odd and even component; for that reason the phase variation is eliminated (Puryear and Castagna, 2008). While shifting the analysis away from the center of the layer, it is necessary to maintain the periodicity in the spectrum. Therefore, the moduli of both components (real and imaginary) of the spectrum, which are not sensitive to phase changes, are computed (Puryear and Castagna, 2008). The shift theorem states that a time sample shifted Δt from the center of the layer t_c in the time domain represents a phase ramp in the frequency domain. Then, the inversion model is derived using the shift theorem and taking general expressions for the real and imaginary part of the complex spectrum. This is simplified in the following expression by Puryear and Castagna (2008):

$$O(t,k) = G(f)\frac{dG(f)}{df} + (2\pi\ T\ k)\sin(2\pi\ f\ T) \tag{4}$$

where *G(f)* is the amplitude magnitude as function of frequency, $k = r_e^2 - r_o^2$, and *O(t,k)* is the objective function at each frequency.

When the sum of the objective function *O(t,k),* which is evaluated at each frequency, is minimized within the range of frequencies in the analysis band, a solution to equation 4 is obtained (Puryear and Castagna, 2008). For each sample frequency there is an associated data term, consequently the method's performance is determined by S/N ratio over a certain analysis band. A more accurate and stable inversion will result if more frequencies and high S/N ratio are present (Puryear and Castagna, 2008).

Searching physically reasonable k and T parameters in a two-parameter model space and minimizing the objective function, a global minimum of equation 4 was found for a given analysis band (Puryear and Castagna, 2008) and the rest of the model parameters can be obtained by:

$$r_o = \sqrt{\frac{G(f)^2}{4} - k\cos^2(\pi\ f\ T)} \tag{5}$$

$$r_e = \sqrt{k + r_o^2} \tag{6}$$

$$t_1 = \frac{1}{2\ i\ \pi\ f} \ln\left[\frac{g(f)}{r_1 + r_2 e^{2i\pi\ f\ T}}\right] \tag{7}$$

The reflection coefficients r_1 and r_2 can be obtained by the summation of the even and odd parts resulting from equations 5 and 6. Equation 7 is obtained by applying the Fourier transform to equation 1 and solving for t_1 (Puryear and Castagna, 2008).

Puryear and Castagna (2008) tested the method using different noise levels of 1 % and 5 %. They concluded that the addition of noise creates instability in the inversion results for very thin layers, because the reflectivity spectrum is almost flat when the thickness approaches zero. Puryear (2006) and Puryear and Castagna (2008) show how to mitigate this problem by applying an arbitrary constraint, where $-0.03 < k < 0.03$, to make sure that the reflectivity pair does not become a single reflection coefficient. Therefore, the strength of the reflection coefficient stays close to what is typically observed on seismic data. All tests were made varying the analysis band and the smoothing filter, demonstrating that the optimal analysis band and filter are controlled by the noise level (Puryear and Castagna, 2008).

2.5.3 Multiple-Layer Case

Considering that a seismogram can be represented as the superposition of impulse pairs. Puryear and Castagna (2008) extended the single-layer case to a general reflectivity series taking into account the frequency spectrum versus time using a time window that can be moved, generating interference patterns at different times which act as a superposition of events. The inversion method simultaneously solves for reflection coefficients and layer thickness for all pairs of reflections, and trace-by-trace, affecting the local seismic response (Puryear and Castagna, 2008).

A reflectivity series r(t) can be represented as the sum of even and odd impulse pairs using the expression defined by Puryear and Castagna, 2008:

$$r(t) = \int_{-\infty}^{\infty}\left[r_e(t) II\left(\frac{t-\tau}{T(t)}\right)\right]dt + \int_{-\infty}^{\infty}\left[r_o(t) I_I\left(\frac{t-\tau}{T(t)}\right)\right]dt \tag{8}$$

where $r_e(t)$ and $r_o(t)$ are the magnitudes of the impulse pairs as a function of time, II is an even impulse pair, I_I is an odd impulse pair and $T(t)$ is the time series of layer time thicknesses. Assuming a seismogram and known wavelet $w(t,f)$, the spectral decomposition of a seismic trace can be expressed as:

$$s(t,f) = w(t,f)\int_{-t_w}^{t_w}\left\{r_e(t)\cos\left[\pi\ f\,T(t)\right] + i r_o(t)\sin\left[\pi\ f\,T(t)\right]\right\}dt \tag{9}$$

where t_w is the window half length. Since the multilayer case involves more than one layer, it is necessary to use an objective function for the inversion process that takes into account the interference between multiple layers (Puryear and Castagna, 2008). Assuming that the wavelet spectrum is known, the objective function $O(t,r_e,r_o,T)$ can be optimized to solve for $r(t)$ and $T(t)$:

$$O(t,r_e,r_o,T) = \int_{f_l}^{f_H}\left[\begin{array}{l} \alpha_e\left\{\mathrm{Re}\left[s(t,f)/w(t,f)\right] - \int_{-t_w}^{t_w} r_e(t)\cos\left[\pi\ f\,T(t)\right]dt\right\} \\ +\alpha_o\left\{\mathrm{Im}\left[s(t,f)/w(t,f)\right] - \int_{-t_w}^{t_w} r_o(t)\sin\left[\pi\ f\,T(t)\right]dt\right\}\end{array}\right]df \tag{10}$$

where f_l and f_h are a low and a high frequency cutoff respectively, α_e and α_o are weighting functions. The ratio of these weighting functions α_o/α_e can be adjusted to find satisfactory results comparing the resolution against noise. For high values of α_o/α_e, the reflectivity inversion results approach the Widess model, where the resolution limit is $\lambda/8$ (Puryear and Castagna, 2008). The time window selected during the inversion will vary according to the desired results. Shorter windows will divide the long series into two isolated even and odd sets, that later will be summed to obtain the longer reflectivity series. Usually this time window is selected by trial and error. If the window is too short, the frequency resolution is lost, and if it is too long the time resolution is compromised (Castagna et al., 2003).

3. FORWARD MODELING

Several synthetic seismic models were tested using the spectral inversion theory described in the previous section. Different parameters were changed on the synthetic wedge models in order to prove that the algorithm performs accurately for diverse case scenarios. The more thoroughly evaluated parameters were the frequency content, noise level, pure even case, and pure odd case. Other parameters, such as the length of the wavelet and stabilization parameter were also tested. After finding acceptable results on the synthetic seismic data, the spectral decomposition and inversion processes were run on a 3D seismic dataset from Alaska.

3.1 Frequency Bandwidth Variation

The synthetic wedge models were built for the single-case scenario of a thin layer. The models consist of convolving different Ricker wavelets of 15, 25, and 35 Hz with a pair of reflection coefficients, where the top reflection value is 0.1 ($r_1 = 0.1$) and the base reflection is equal to ($r_2 = -0.075$). The synthetic seismic models consists of 200 samples at a sample rate of 1ms (200 ms total time length) on a hundred (100) traces that range from 0 to 100 ms time thickness. The polarity used for the models is red for an increase in impedance (positive) and blue for decreasing impedance (negative).

The predominant frequency variation of the source wavelets was designed for 2 functions. First, to emulate the loss of frequency content that real seismic data frequently exhibits due to attenuation, transmission loss, etc. Second, it was used to evaluate the power of resolution of the spectral inversion process when frequency content is low. Moreover, random noise was added to the models in two different scenarios and for every wedge with different central frequency. The first scenario presents almost no noise (0.01 %) and it is defined as the high S/N case. In the second case, 1 % random noise was added and it is defined as the noise case. These scenarios allow evaluation of the reliability of the inversion when noise is present.

3.1.1 Synthetic Wedge Model with Central Frequency at 35 Hz

Wedge models were built with a central frequency of 35 Hz shown on figure 16 for the high S/N (noise = 0.01 %) and on figure 18 for the low S/N case. The inversion process involves wavelet extraction using different wavelengths and with different time windows. During the inversion process, diverse α parameters (the alpha parameter is based on the ratio of the weighting functions described above) were tested until the most stable solution was found. Results were frequently compared and evaluated to select/adjust the parameters that satisfy and generated a solution that improves resolution.

For both cases the wedge was resolved (Figure 17 and 19). The method of spectral inversion described before (Puryear and Castagna, 2008) solved both reflection

coefficients below the tuning thickness without adding or boosting any noise present in the data, remarkably improving the seismic vertical resolution on the high S/N case. It can be observed that for the inversion result of the noise case (Figure 19), the background looks slightly different than the one with high S/N relationship (Figure 17). The presence of noise in the model is beginning to affect the background, but it is not perturbing the overall solution at this point.

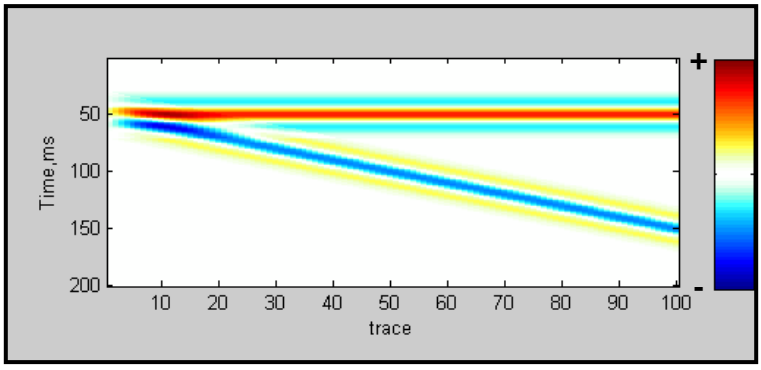

Figure 16: Wedge model with a central frequency of 35 Hz with random noise = 0.01%. The sample rate is 1 ms with 100 traces that also represent the time thickness.

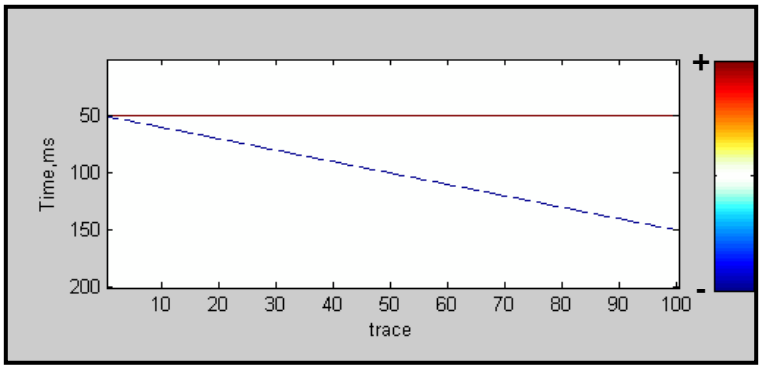

Figure 17: Spectral inversion result from the wedge model from figure 16. The wedge model is perfectly predicted by the inversion method.

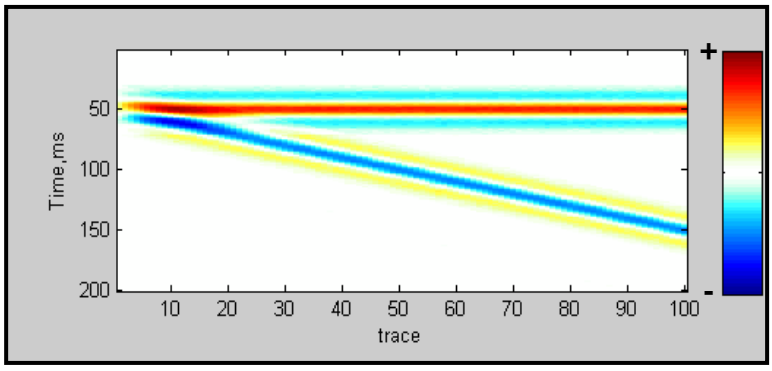

Figure 18: Wedge model with a central frequency of 35 Hz with random noise = 1.0%. The sample rate is 1 ms with 100 traces that also represent the time thickness.

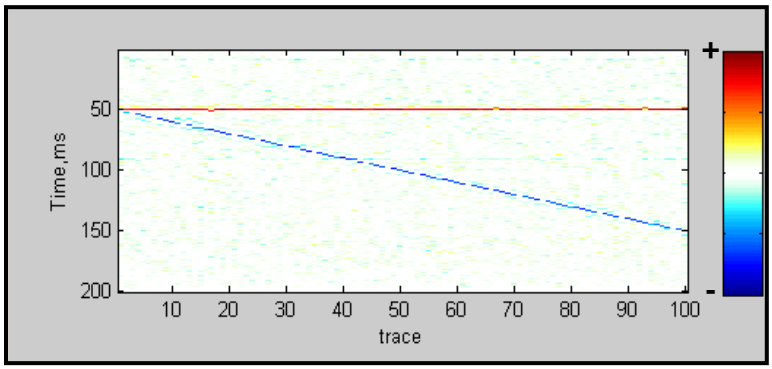

Figure 19: Spectral inversion result from the wedge model from figure 18. The wedge model is perfectly predicted by the inversion method.

When imperfect wavelets are estimated (shape, phase, and wavelength), the results can be unstable and imprecise (Figure 20a). If the wavelet extraction is more precise, then better inversion results can be obtained (Figure 20b). Decreasing the stabilization parameter (alpha-weighting parameter) can lead to results where the wedge model can be resolved (Figure 21), but the background solution is unstable. The noise is slightly boosted in the background during the inversion, because the weighting parameter expands the bandwidth. The geophysicist has to make a decision at this stage as to how far the frequency band can be or wants to be expanded.

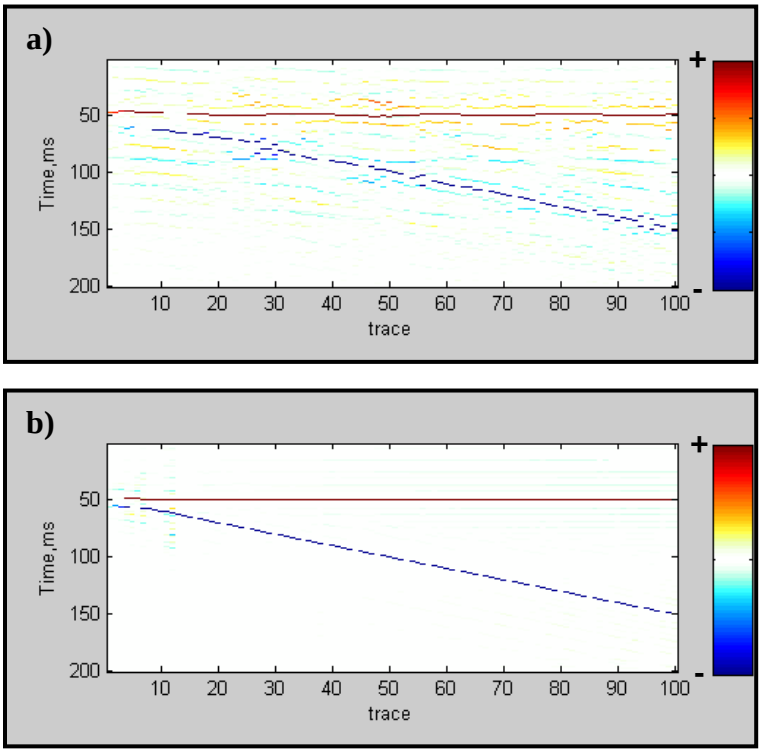

Figure 20: Spectral inversion result from the wedge model from figure 18. The wavelet length and shape are not well estimated; therefore the solution is totally unstable (a). Subsequently, if the wavelet extraction is performed more accurately (wavelength and shape); the results are improved (b) but the wedge is still not resolved.

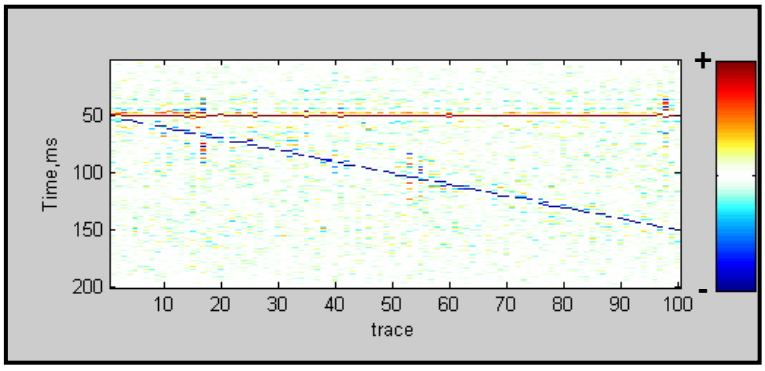

Figure 21: Spectral inversion result from the wedge model from figure 18. The wedge is resolved compare with figure 20, but the overall background solution is unstable. The need to broaden the bandwidth is also boosting the noise due to the reduction on the stabilization parameter.

3.1.2 Synthetic Wedge Model with Central Frequency at 25 Hz

The second scenario involves a decrease of the frequency content. The synthetic wedge models were convolved using a Ricker wavelet of 25 Hz for both cases, high S/N (Figure 22) and with the presence of noise (Figure 24). For the high S/N case the results show that the wedge is resolved (Figure 23). For the noisy case, the prediction of the reflection coefficients for the wedge model are also solved (Figure 25); nevertheless, the background from this result compared with the inversion from the noisy 35 Hz wedge model case (Figure 19) looks similar. There is a small increase of the background noise that makes it more difficult to distinguish both top and base reflections. This means that the inversion process works perfectly for seismic data with a high S/N ratio, even though the frequency content was reduced from a central frequency of 35 Hz to 25 Hz.

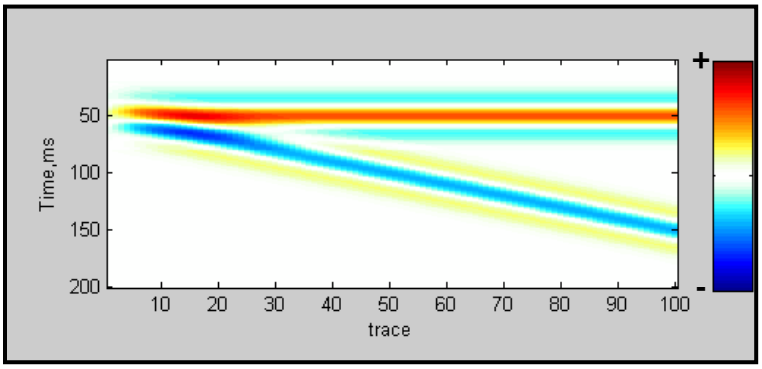

Figure 22: Wedge model with a central frequency of 25 Hz with random noise = 0.01%. The sample rate is 1 ms with 100 traces that also represent the time thickness.

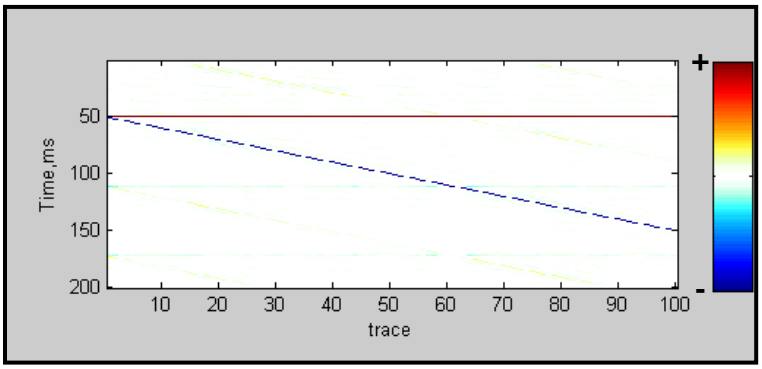

Figure 23: Spectral inversion result from the wedge model from figure 22. The wedge model is perfectly resolved by the inversion method.

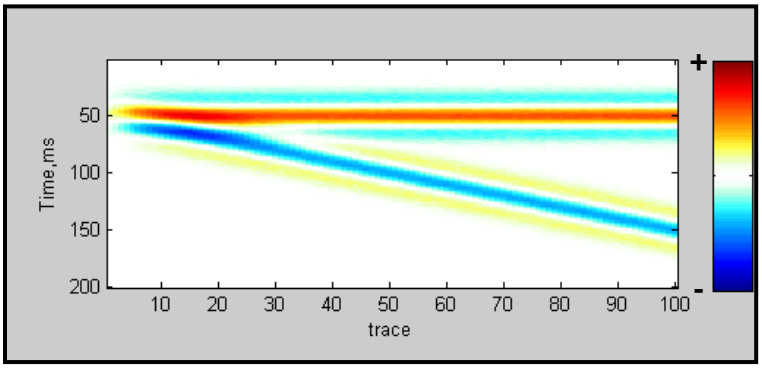

Figure 24: Wedge model with a central frequency of 25 Hz with random noise = 1.0%. The sample rate is 1 ms with 100 traces that also represent the time thickness.

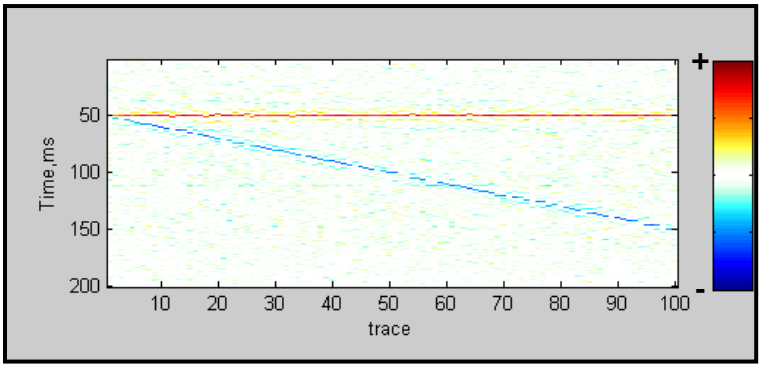

Figure 25: Spectral inversion result from the wedge model from figure 24. The wedge model is resolved, although the background presents a noise boost that makes more difficult to distinguish both top and base reflections.

3.1.3 Synthetic Wedge Model with Central Frequency at 15 Hz

The third scenario involves another decrease of the frequency spectrum. The synthetic wedge models were convolved using a Ricker wavelet of 15 Hz for both cases, high S/N (Figure 26) and with the presence of noise (Figure 28). For the high S/N case, the results obtained are again perfect and the wedge is resolved (Figure 27). For the noisy case, the reflection coefficients predicted by the inversion method are solved (Figure 29). Comparison of this result, alongside the previous inversion results from the same noisy data (Figures 19 and 25), shows another a significantly increase of the background noise, but the wedge still can be clearly resolved and defined. This means that the inversion process works perfectly for seismic data with a high S/N ratio with a frequency content of 15 Hz. On the other hand, the need of broadening the spectrum to resolve the synthetic wedge boosts significantly the noise that was added to the initial model.

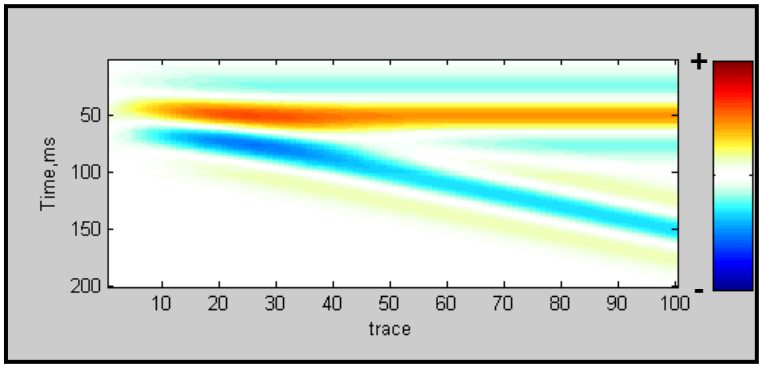

Figure 26: Wedge model with a central frequency of 15 Hz with random noise = 0.01%. The sample rate is 1 ms with 100 traces that also represent the time thickness.

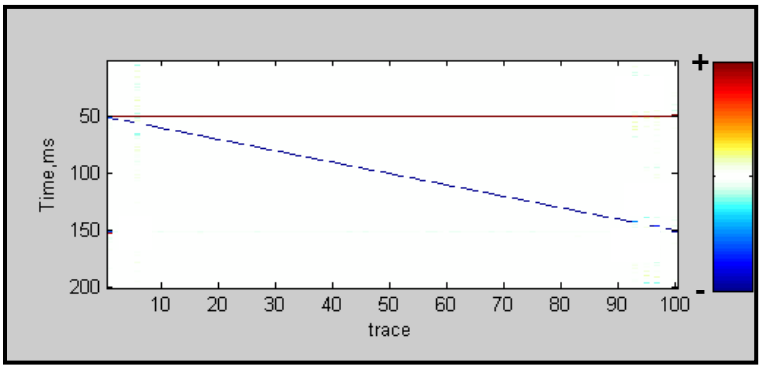

Figure 27: Spectral inversion result from the wedge model from figure 26. The wedge model is perfectly predicted by the inversion method.

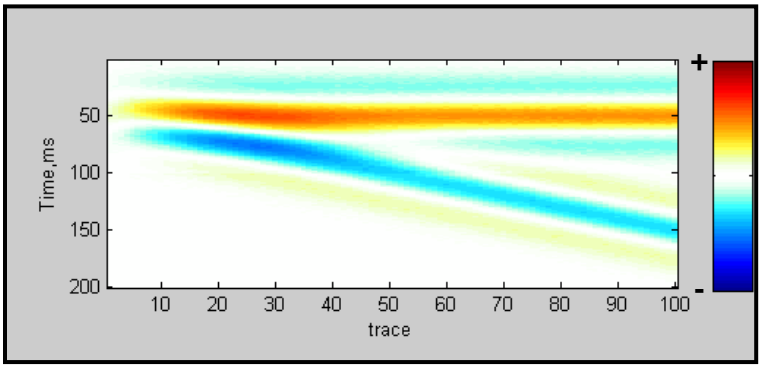

Figure 28: Wedge model with a central frequency of 15 Hz with random noise = 1.0%. The sample rate is 1 ms with 100 traces that also represent the time thickness.

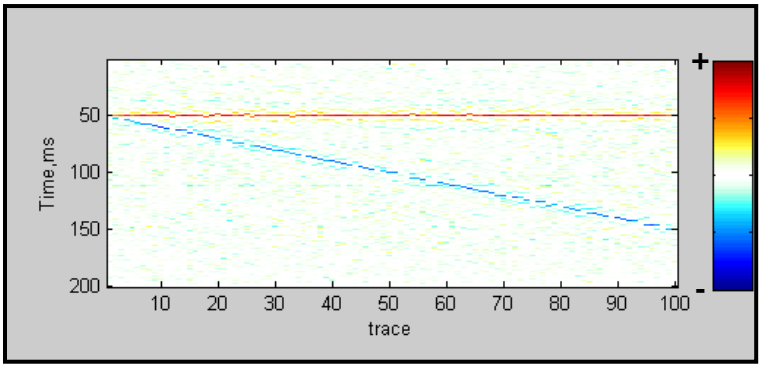

Figure 29: Spectral inversion result from the wedge model from figure 28. The wedge model is resolved, although the background presents a significantly noise increase that makes even more difficult to distinguish both top and base reflections.

3.2 Special Wedge-Model Cases

When conducting these tests to evaluate if the method is able to perform correctly, there were two additional cases that needed to be tested. The first one is the even component scenario; the second case is an exact description of the odd component scenario. Because, it was proved in the previous tests that the frequency content did not significantly affect the results, both wedge models were created using a Ricker wavelet of 35 Hz. The high S/N ratio was selected to run these models at 0.01% noise level to simplify the tests, because the vertical resolution and wedge models were predicted accurately.

3.2.1 The Pure Even-Component Case

The synthetic wedge model was built using a pair of reflection coefficients with the same magnitude and polarity (positives) values of 0.1 ($r_1 = 0.1 = r_2$) and convolved with a Ricker wavelet of 35 Hz (Figure 30). The synthetic seismic models consist of 200 samples at a sample rate of 1ms (200 ms total time length) on a hundred (100) traces that range from 0 to 100 ms time thickness. The polarity used for the models is red for an increase in impedance (positive) and blue for decreasing impedance (negative). The results obtained from the inversion are perfect and the wedge is resolved (Figure 31). Given that, the theory described says that the even component contributes more to the

solution below the tuning thickness. Therefore, this result confirms the theory and the performance of the spectral inversion algorithm.

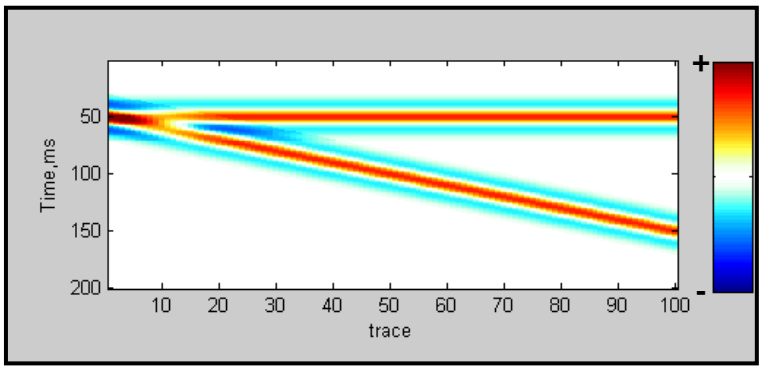

Figure 30: Pure even-component case scenario ($r_1 = 0.1 = r_2$) for a wedge model with a central frequency of 35 Hz with random noise = 0.01%. The sample rate is 1 ms with 100 traces that also represent the time thickness.

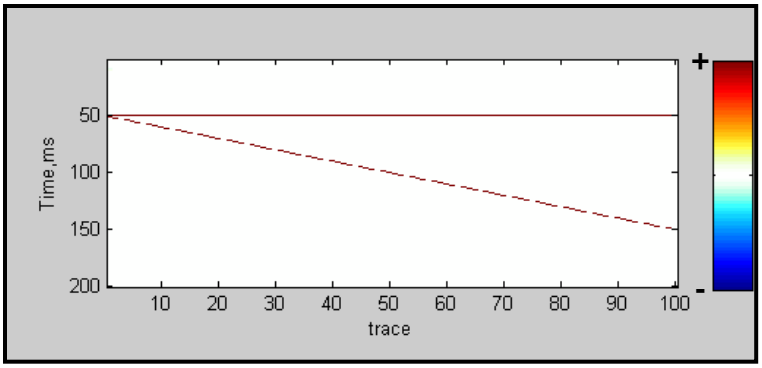

Figure 31: Spectral inversion result for the pure even-component case from figure 30. The wedge model is perfectly predicted by the inversion method as was expected.

3.3.1 The Pure Odd-Component Case

The synthetic wedge model was built using a pair of reflection coefficients with the same magnitude value of 0.1 but opposite polarity (r_1 = 0.1 and r_2 = -0.1) and convolved with a Ricker wavelet of 35 Hz (Figure 32). The results obtained from the inversion are also accurate and the wedge is resolved (Figure 33). This means that even for the odd case, where the theory states that the even component contributes more to the solution below tuning, nevertheless the algorithm recovers the vertical resolution completely.

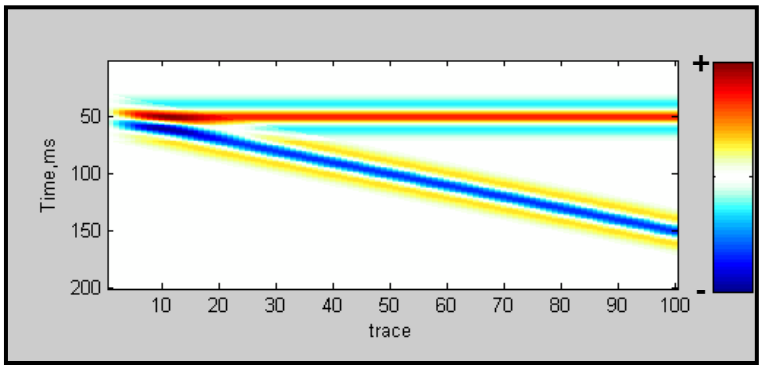

Figure 32: Pure odd-component case scenario (r_1 = 0.1 and r_2 = -0.1) for a wedge model with a central frequency of 35 Hz with random noise = 0.01%. The sample rate is 1 ms with 100 traces that also represent the time thickness.

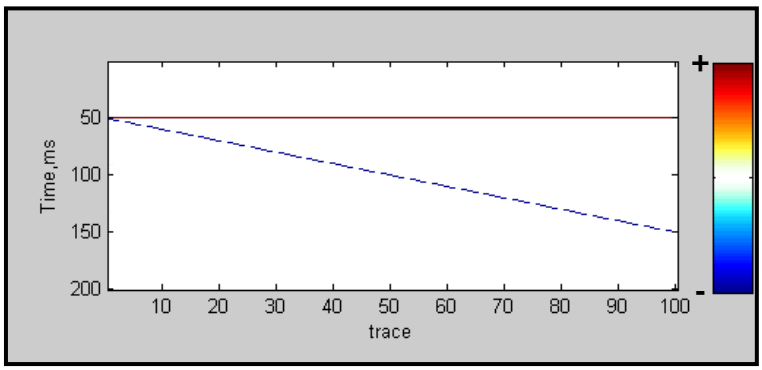

Figure 33: Spectral inversion result for the pure odd-component case from figure 32. The wedge model is perfectly predicted by the inversion method.

A case similar to these examples, in which both amplitude values are equal in magnitude with the same or opposite polarities, is hard to find in real seismic data, especially if the amplitudes are preserved at 32 bits for processing. However, it was worth trying to test the performance and stability of the algorithm.

From these tests it can be observed that the frequency content of the synthetic data did not affect the inversion results, as solved all the wedges with a high S/N ratio. On the other hand, these studies showed that just a small increment of noise (1 %) can affect the performance of the inversion process.

Even though all synthetic wedges were well predicted, the need for expanding the frequency bandwidth to increase the vertical resolution also boosts the noise, especially when the bandwidth is lower in frequency content. Therefore, if the vertical resolution is to be improved by any inversion technique, it is important to eliminate the noise as much as possible during processing. In addition, it was demonstrated that there is a high probability to produce poor results (vertical resolution improvement) when the wavelet is not accurately extracted and applied during the inversion process.

4. DATASET

The area under study is located within the Cook Inlet Basin of Alaska (Figure 34). The dataset consists of a 3D seismic survey that covers approximately 18 km^2 of the Cannery Loop oilfield. Eleven (11) highly deviated wells have been drilled in the Cannery Loop oilfield at different target depths that range from 1200 to 3600 m. The oilfield is a simple anticline that extends over 5 kilometers in the northwest-southeast direction and is around 3 kilometers east-west. There is one major fault located at the southeast of the structure that separates the Cannery Loop gas accumulations from the Kenai field (Brimberry et al., 2001).

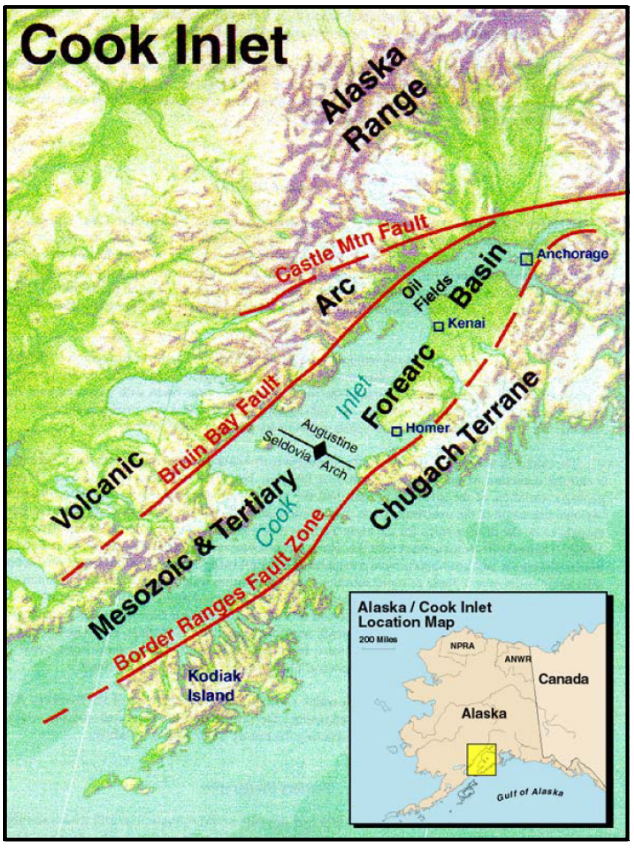

Figure 34: Present-day geometry of the Cook Inlet Basin geomorphology and regional tectonic boundaries (from Swenson, 2001).

4.1 Geological Setting

The Tertiary Cook Inlet Basin covers an area of 102,000 square km that extends from the Matanuska Valley south along the Alaskan peninsula in a north-east direction (Figure 34). The basin is set in a fault-bounded NE-SW elongated forearc, and exhibits complex stratigraphy due to the variable uplift/subsidence rates that caused thickness variations of a hundred meters (Figure 35) over the Tertiary Period (Swenson, 2001). There is also lithologic complexity due to the different provenance rocks and the depositional systems (Figure 35) (Hayes et al., 1976).

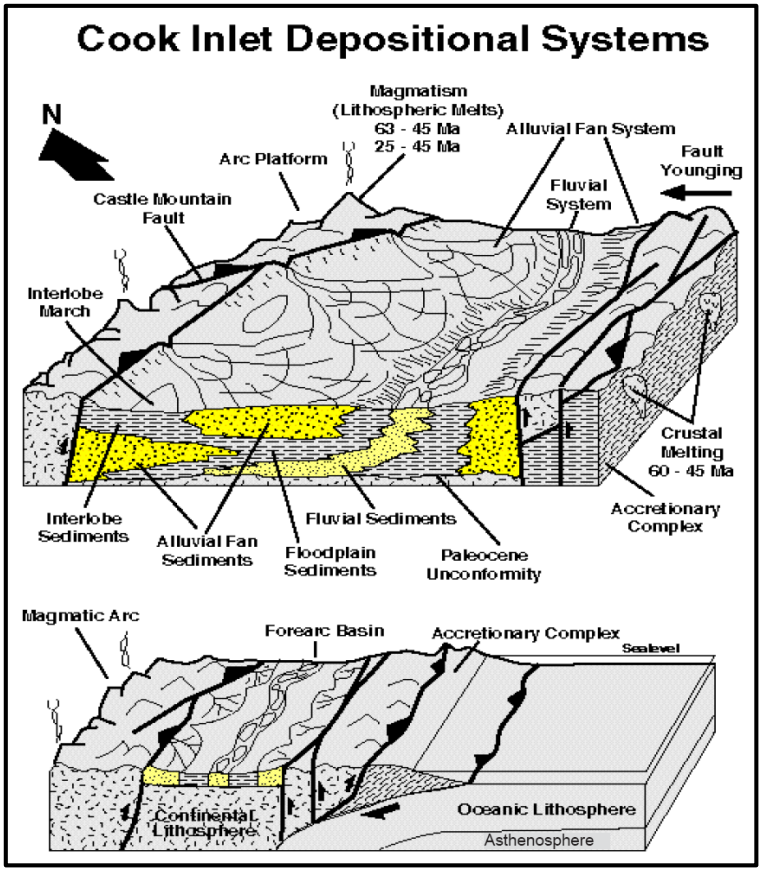

Figure 35: Cook Inlet basin depositional model (from McGowen, et al., 1994, in: Swenson, 2001).

4.2 Stratigraphy

The stratigraphic intervals with economic potential for gas exploitation are encompassed by the Tyonek, Beluga, and Sterling formations, deposited during the Late Oligocene, Miocene and Pliocene (Figure 36) in a non-marine environment. The focus of this study is the upper Beluga and Sterling Formations which, at present, are major gas producers from the Cook Inlet Basin.

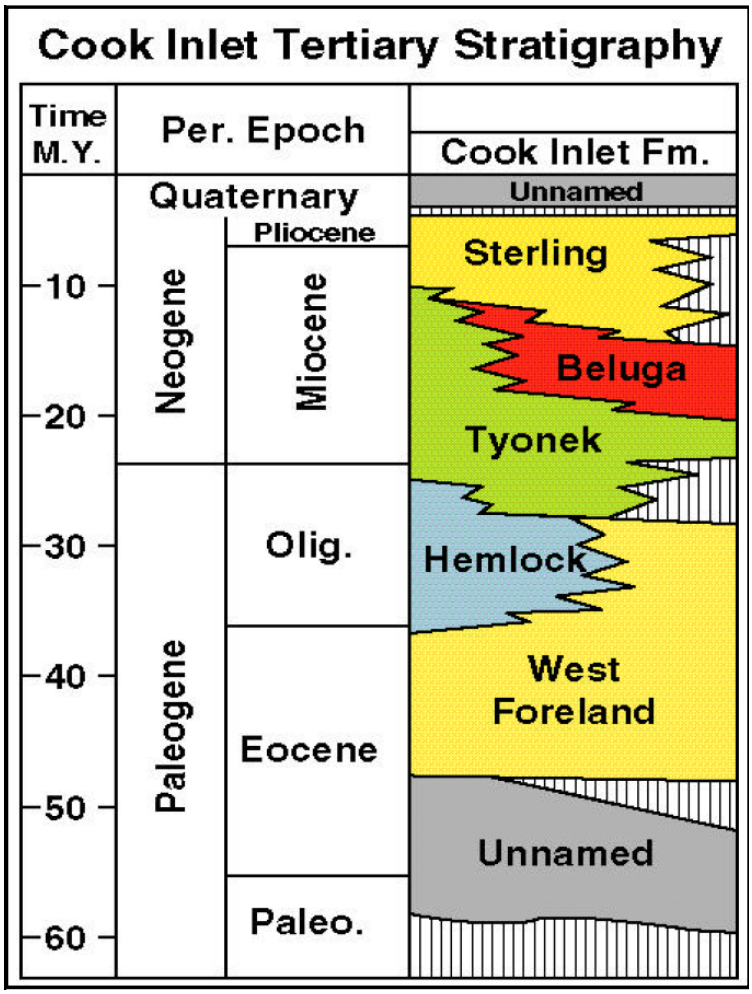

Figure 36: Generalized stratigraphic chart of the Cook Inlet Basin (from Swenson, 2001).

4.2.1 Beluga (Miocene)

This formation is a thick (over 900 m) siltstone-rich unit where channelized muddy sandstones, coal, and tuff beds are common (Swenson, 2001). The coarser facies are constituted predominantly by metamorphic rock fragments and quartz derived from the Kenai-Chugach Mountains to the east (Hayes et al., 1976; Brimberry et al., 2001). Sand body thickness can vary from 1.5 to 9 m and porosities from 5 to 20%. The coal beds in the Beluga Formation, in contrast to the underlying formation, are mostly thin (<1.5 m) and of limited areal coverage. The overall Beluga section is compacted and the reservoir sands are too thin to resolve with seismic data.

4.2.2 Sterling (Miocene-Pliocene)

The Sterling Formation represents deposits of much larger meandering streams originating from the north/northwest. It comprises stacked fluvial channels, mud drapes, siltstones, and local thin coal beds (Hayes et al., 1976; Brimberry et al., 2001). Sandstone deposits are friable, moderately well sorted, poorly consolidated fine to coarse-grained sandstones, consisting of abundant volcaniclastics, glass shards, quartz, and feldspar (Swenson, 2001; Brimberry et al., 2001). Productive sandstone sequences typically range from 9 to 18 m thick; some are more than a 30 m thick. Porosities vary between 20 and 30%. Presence of abundant coal and absence of massive sands mark the regional unconformity identified as the base of the Sterling Formation.

4.3 Analog Cases

Understanding modern analog environments allows coherent qualitative information that can aid subsurface interpretation using seismic data. Therefore, following the description and definition of the paleo-environments for the Beluga and Sterling formations in the literature, it was necessary to find recent examples that show how meandering and/or braided systems behave.

Bridge (2006) shows some good examples and descriptions of different rivers around the world. The supposition that the ratio width to thickness (W/T) of braided channels is greater than in meandering channels is not always correct, as channel belts from the meandering Mississippi and braided belts from the Brahmaputra have the opposite relationship; the Mississippi has a W/T = 15km/40m = 375, while the Brahmaputra has a W/T = 10 Km/40 m = 250. Meandering and braided channels have curved channel segments adjacent to compound bars and also migrate by erosion of concave banks and deposition of compound bars. In some cases, there is even accretion of point and braid bars during floods, as can be seen in the Sagavanirktok channel belt in northern Alaska (Figure 37) and in an example of a GPR profile, where dramatic lateral changes can be observed (Figure 38).

Figure 37: Modern braided and meandering channels system example from Sagavanirktok River, northern Alaska. A channel belt with compound braid and point bars associated with meandering, anastomosing and braided- meandering channels separated by a bar assemblage. The channel is 2 km wide (from Bridge, 2006).

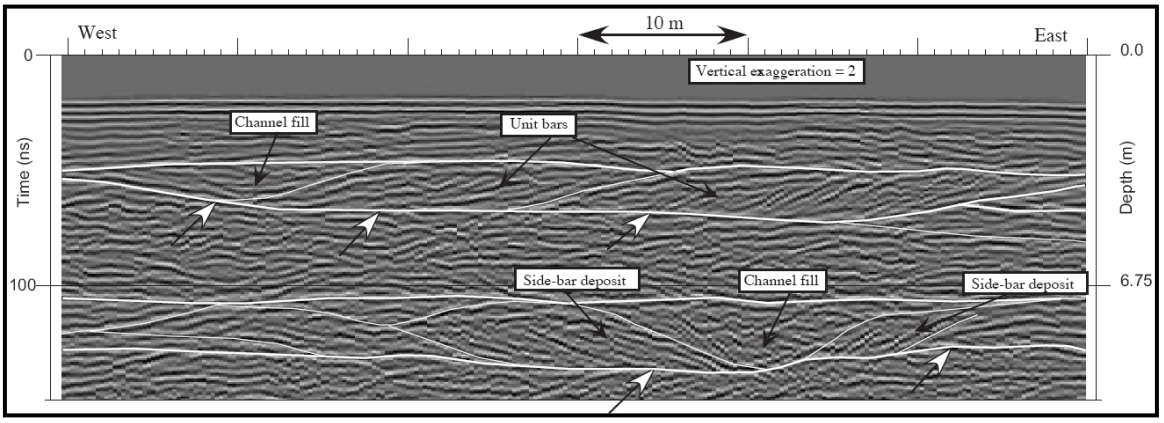

Figure 38: GPR profile through braided and meandering river deposits of the Sagavanirktok River, Alaska. It shows (upper) compound bars with large-scale inclined strata dipping (unit bars), lower in the profile a confluence fill is bounded on both sides by side (point) bars (from Bridge, 2006).

5. CASE STUDY RESULTS

The reflectivity inversion and spectral decomposition methods were applied using a full stack seismic dataset. Although, the subsurface does not show any structural complexity, the quality of the seismic data is poor, due to the proximity of the Kenai River which generates static and acquisition problems, and partial amplitude dimming (Figure 39). Well logs were provided from several wells, including sonic, induction, density, GR, and SP logs, but just 3 wells out of 11 had a complete suite over the section of interest.

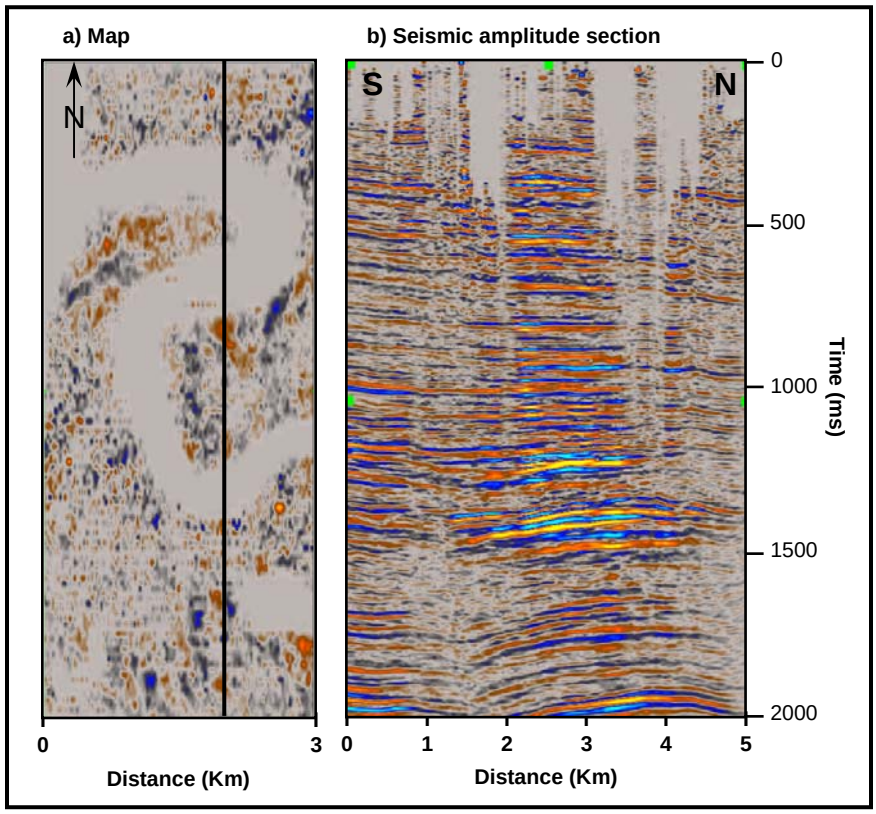

Figure 39: Map showing the position of the Kenai River within the survey (a). The seismic data was affected by the river during acquisition. It is observed in seismic section (b) some vertical areas where the amplitudes are really affected.

5.1 Phase Analysis and Conversion

The phase of the seismic data can be checked, correlated, and corrected using synthetic seismograms (well ties), comparing the impedance response due to the main geological units. Three (3) synthetic seismograms were generated using the sonic and density logs from each well and the only check shot available in the oilfield. The best synthetic tie for the upper section of the Sterling and Beluga formations is shown in figure 40. The seismic-data polarity is defined as a peak for an increase in impedance (blue) and a trough as a decrease in impedance (red). The wavelet was statistically extracted from the seismic (Figure 41) along the well path.

Several synthetic seismograms were also created using synthetic Ricker wavelets with different frequency contents of 20, 25, and 35 Hz (Appendix A). For most of the wells (9) a synthetic seismogram was generated and correlated with the seismic, but there were just 3 wells where the results were fairly good (due to not only the log and seismic quality but also the highly deviated well paths) within the Sterling and upper Beluga formations. For that reason these were used in the study. After detailed synthetic analysis it was concluded that it was necessary to apply a -180 degree phase rotation to correct the assumed zero phase of the seismic data. In general, the quality of the tie was good but limited due to the relatively low S/N ratio of the seismic. The correlation coefficient for the tie was 0.77 using a time-window analysis that ranged from 800 to 1300 ms (Figure 40).

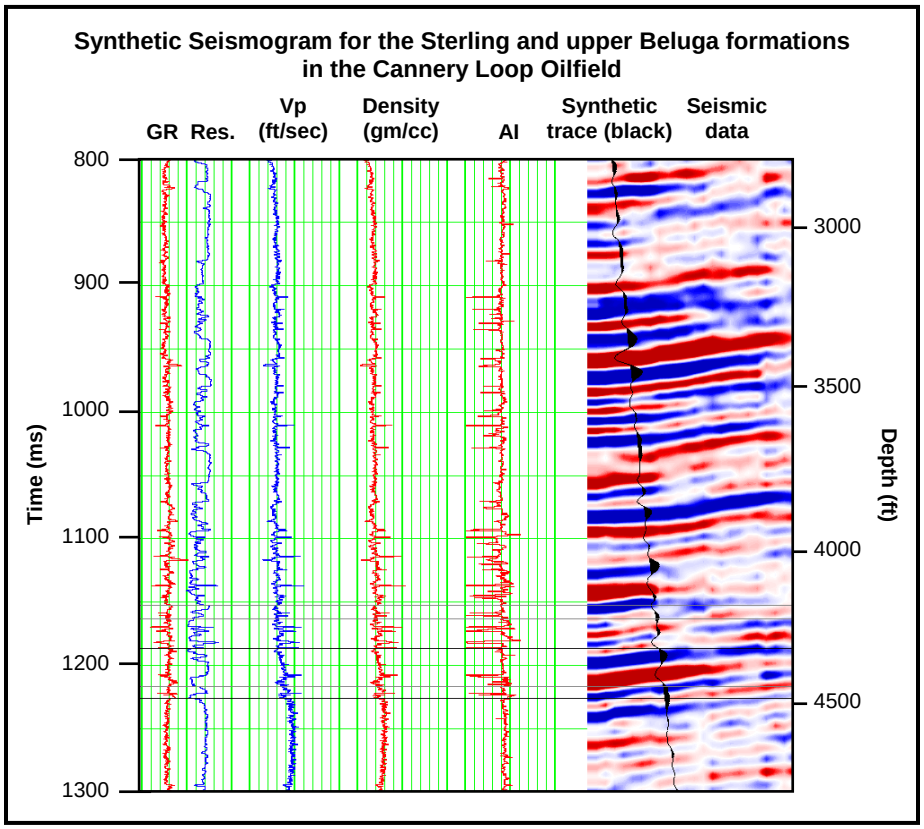

Figure 40: Synthetic seismogram for the Sterling and upper Beluga formations in the Cannery Loop oilfield.

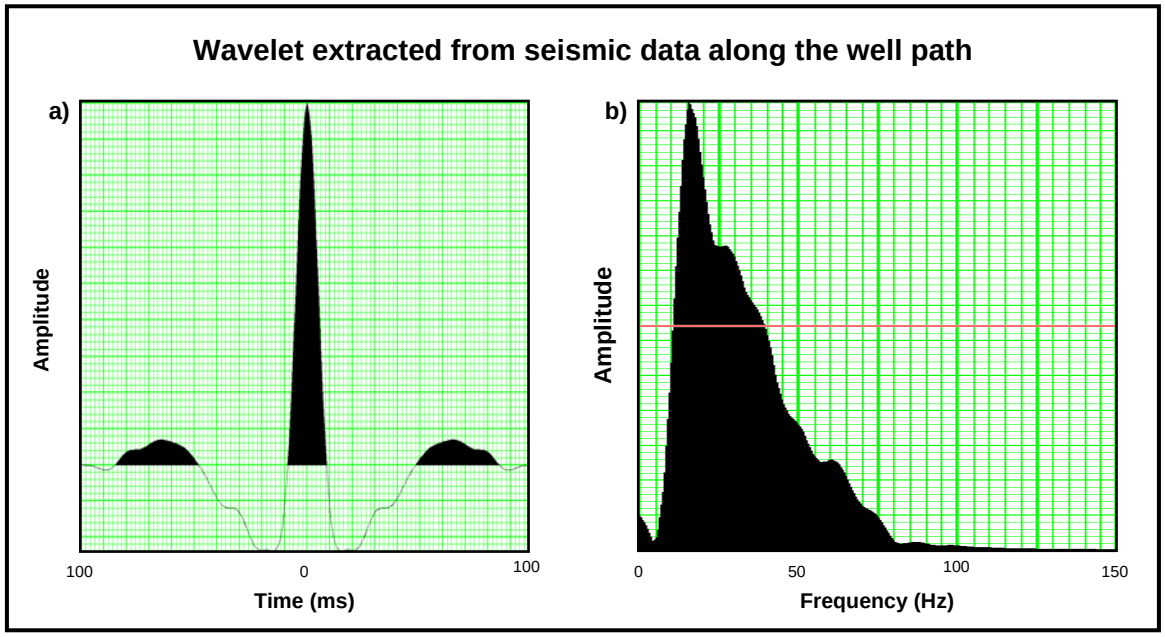

Figure 41: Wavelet extracted from seismic data (a) and its spectrum (b) along the well used in figure 40.

5.2 Wavelet Characterization and Spectral Inversion Process

During the spectral inversion process, the extraction of the wavelets that best characterize the seismic response, as well as the selection of the stabilization factor of the inversion are important (Chopra, et al., 2006). Even though it was determined that there is no need for external constraints (well data, initial model, and layering) beyond the seismic data input, the results were validated using the well that showed the best tie.

Once the data are phase corrected and resampled to 1ms, the wavelet extraction process is initiated. A statistical extraction is performed using different windows in the target zone (700 ms to 3500 ms) to characterize the vertical behavior of the wavelet. Figure 42 shows the average amplitude spectrum for the raw seismic data in the time-window analysis mentioned before. A 400 ms long wavelet was selected to characterize most of the possible side lobes in the data. As part of the process, the estimation of different time-variant wavelets is executed to understand variation of the amplitude spectrum with time/depth (Figure 43).

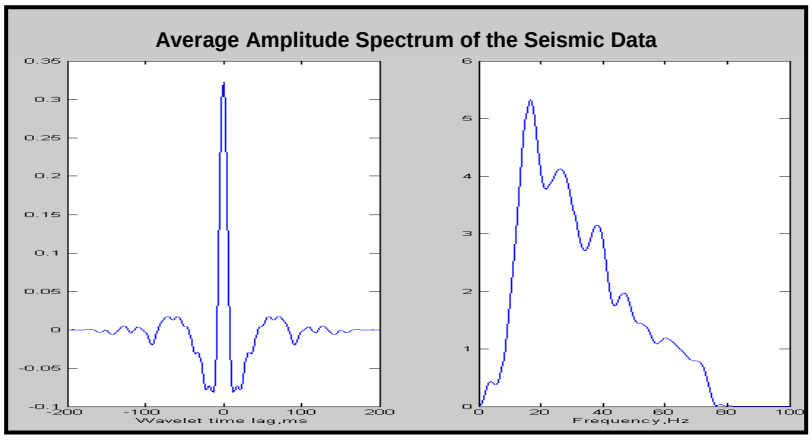

Figure 42: Average amplitude spectrum from the raw seismic data.

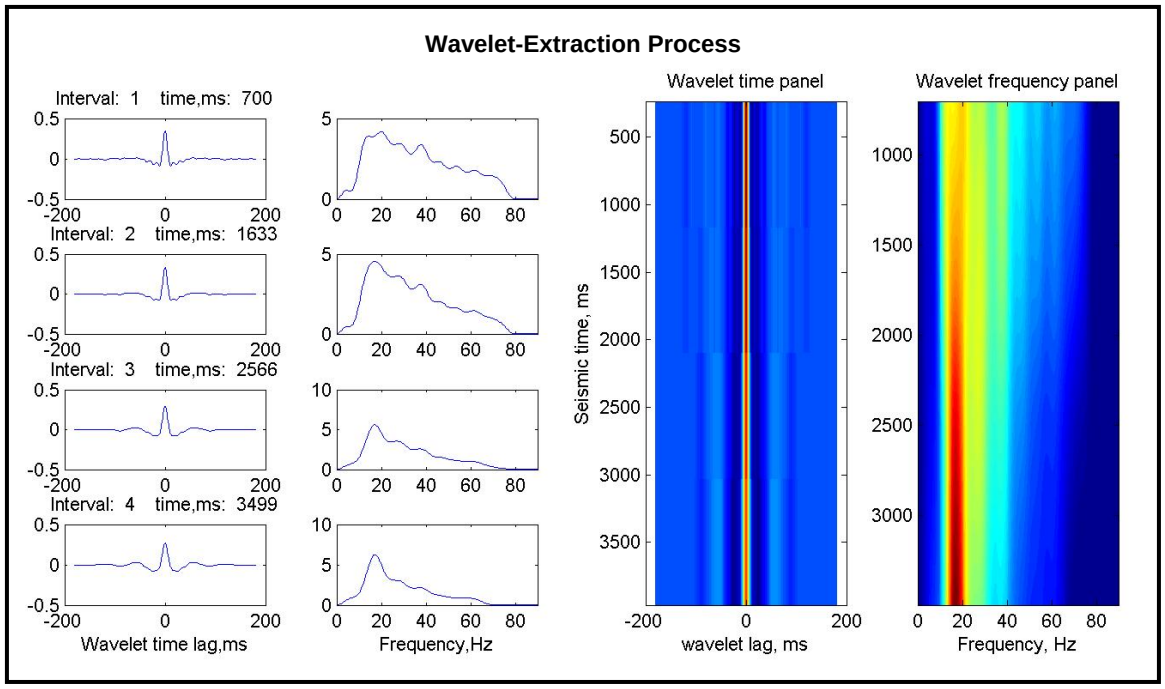

Figure 43: Wavelet-extraction process showing the wavelet amplitude spectrum variation as a function of time. The length of the wavelet is 360 ms.

The most stable spectral inversion results are obtained using wavelets containing most of the side lobes and with the shortest length that still preserves the amplitude spectrum of the wide wavelength. It shows that a wavelet with a length of 360 ms (figure 43) contains a similar amplitude spectrum to the previous wavelet of 440 ms (see Appendix B). For smaller wavelengths, the amplitude spectrum is imprecise and the quality of the spectral inversion is reduced, consequently the use of smaller wavelets is discarded.

Part of the wavelet characterization process is to divide the target zone (700 to 3500 ms) into different intervals to evaluate the variation with time. The zone was divided into 7 intervals, with an increment of 1 interval (Figure 44). Generally, when the

number of intervals is increased, more detail is observed regarding the changes in wavelet shape and spectrum with time. In this case, for an interval division of 4 (Figure 43) sudden changes occur within the second and third interval, while at interval of 7, the changes are smoother in frequency content. Therefore, an interval division of 7 was selected, as it is the simplest wavelet that contains sufficient detail about the spectrum variation with time.

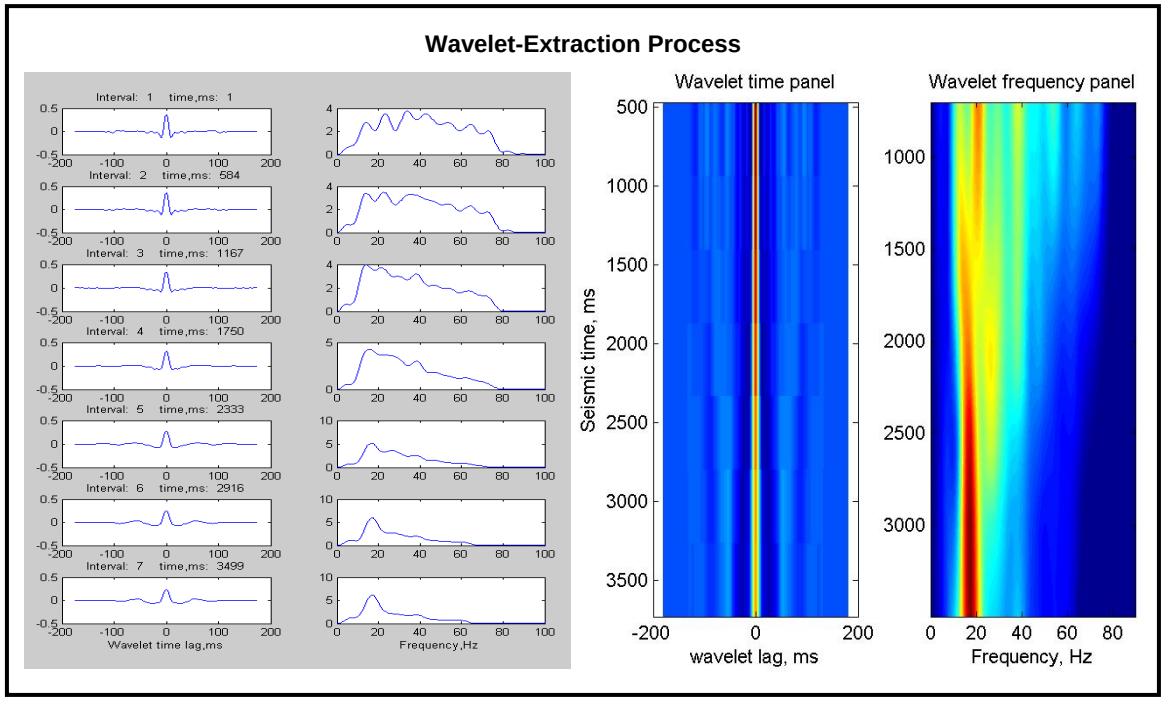

Figure 44: Wavelet-extraction process showing the wavelet amplitude spectrum variation as a function of time in seven different intervals. The wavelength is 360 ms.

5.3 Spectral Inversion Results

With the wavelet characterization finished, several spectral inversion tests were run in a small area around the well (this is where well information is important) to select the proper stabilization parameter. These results showed different vertical resolutions and hence diverse S/N ratios (see chapter 3). The parameter value selected is the one that produced the most stable results, least noise increase, and the best well tie.

Once the parameter is chosen, the spectral inversion is implemented on the whole seismic survey within the time window that was selected previously. Comparing seismic data volumes (Figure 45), amplitude, and reflectivity respectively, it is observed that the resolution has improved while the main events are still preserved. The polarity used is an increase in impedance represented by a peak (black) and a decrease by a trough (red).

An average frequency spectrum comparison of the original seismic data and the reflectivity volume shows how the frequency band was broadened (Figure 46). Notice how the frequency band between 0-80 Hz is flattened as should be expected when the footprint of the wavelet is removed by the inversion.

It is fundamental to have a quality control process of the results. Because the frequency band is expanded, the most important quality control or test is to compare side-by-side the original seismic and the results of the inversion, applying a band-pass filter similar to the frequency spectrum of the original seismic record (Figure 47). This is

similar to convolving the reflection coefficients with a wavelet that in this case is perfectly known.

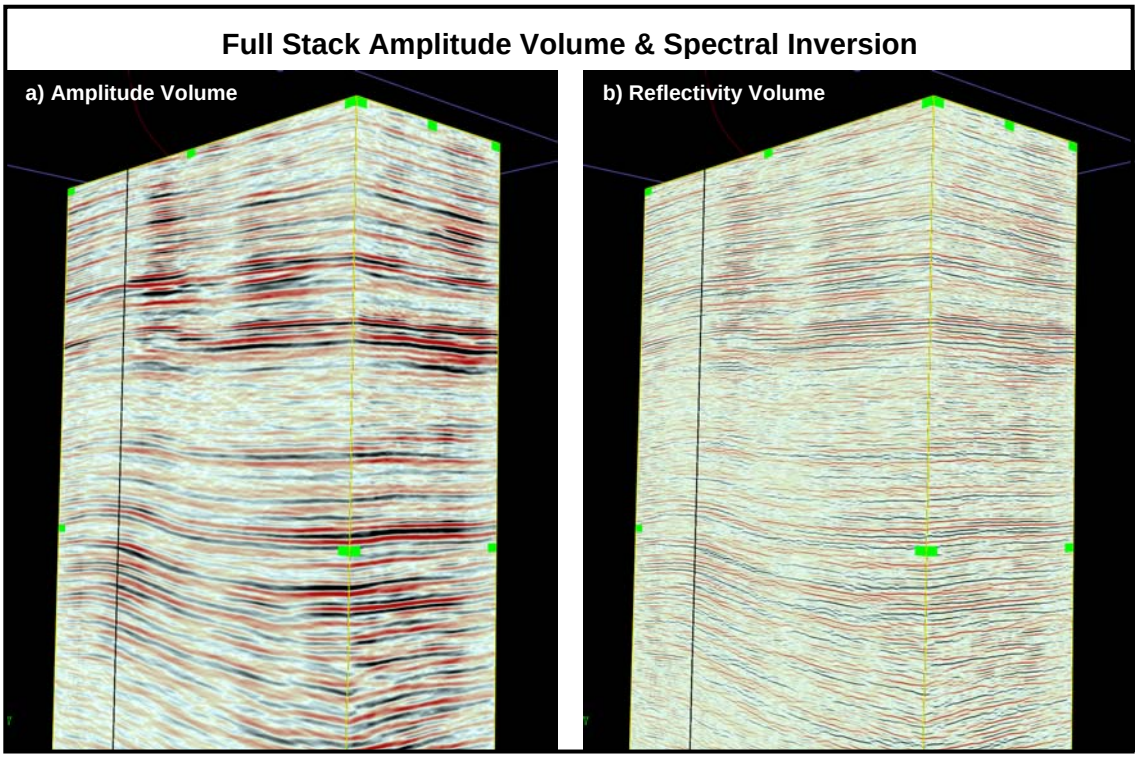

Figure 45: Comparison of the full stack amplitude and the spectral inversion volume. Notice the increase in resolution while preserving the main events.

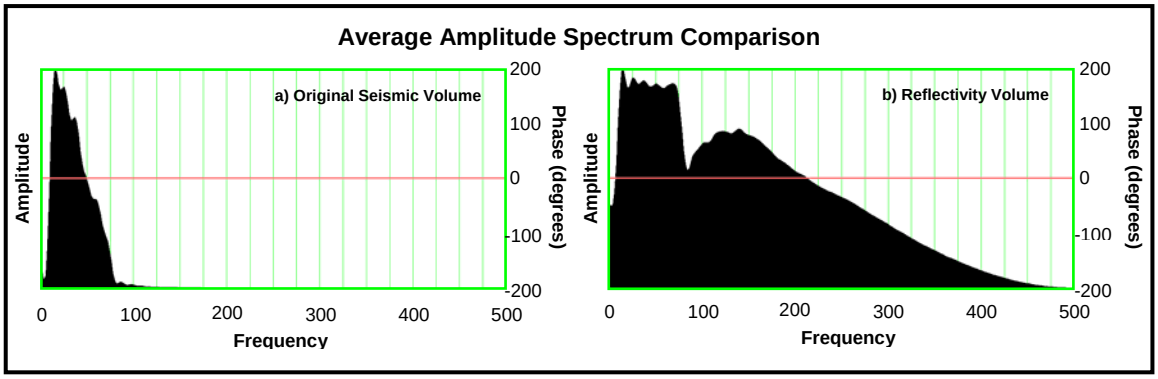

Figure 46: Average amplitude-spectrum comparison of a) the full stack amplitude volume and b) the spectral inversion. The frequency band is broadened; notice the flat shape at lower frequencies (10-80 Hz) due to wavelet removal.

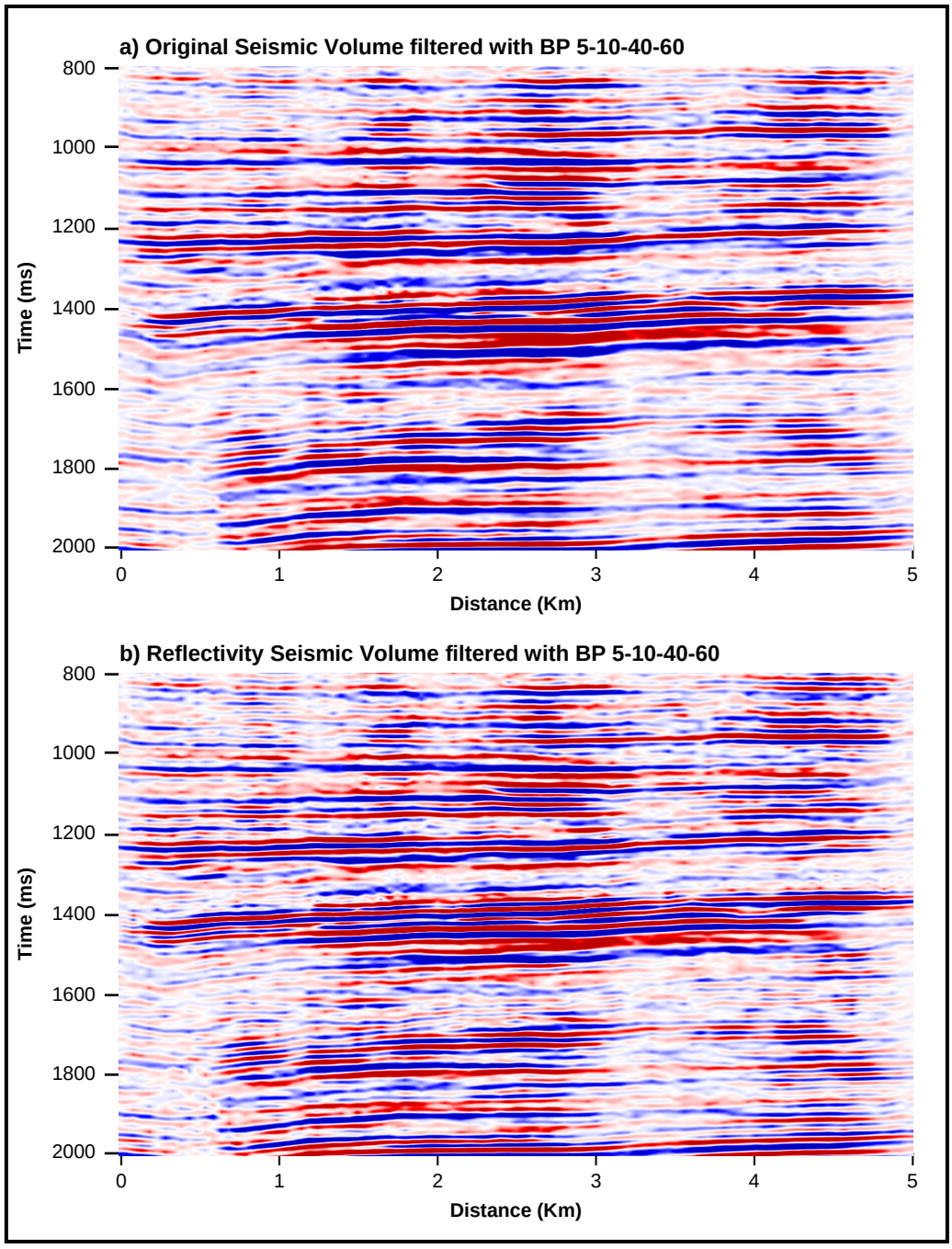

Figure 47: Comparison of a full stack amplitude and spectral inversion section with a band-pass filter of 5-10-40-60 frequency range. Both seismic sections seem to be very similar, demonstrating the spectral inversion process is not adding any noise or artifacts to the original data.

A band-pass filter, defined with a frequency range of 5-10-40-60, was applied to both seismic volumes (original and inverted) just to be sure that the same frequency content is comparable. The results on a particular seismic section (Figure 47), demonstrate that the original seismic and reflectivity volumes look approximately the same. For that reason the spectral inversion process does not appear to be adding any noise or artifacts to the original data.

The inversion results are also compared side-by-side against synthetic seismograms. This is another way to visualize the improvements in the vertical resolution and consistency of the inversion process. Figure 48 shows a set of logs (GR, Resistivity, Vp, Vs, and Impedance), and three seismic sections with their respective synthetic seismograms for different frequency content. Figure 49 shows a closer look at the bottom section (1275-1450 ms). The correlation of the original amplitude seismic section with the synthetic seismogram from the well shows a good tie, with a correlation coefficient of r = 0.71 for the section between 800ms - 1250ms (Figure 48a). For the time window used in figure 49a (1325 ms – 1450 ms) the correlation is 0.54.

The second seismic image and well tie (Figure 48b and 49b) is a band-limited reflectivity section, with frequency content of 5-10-150-210 Hz. This same bandwidth was used to generate a wavelet which was convolved with the reflectivity computed from the logs. The results from the well tie look qualitatively similar to the original seismic tie (Figure 48a and 49a), except that the correlation analysis is lower for both time windows described before, r = 0.31 (Figure 48b) and r = 0.27 (Figure 49b) respectively.

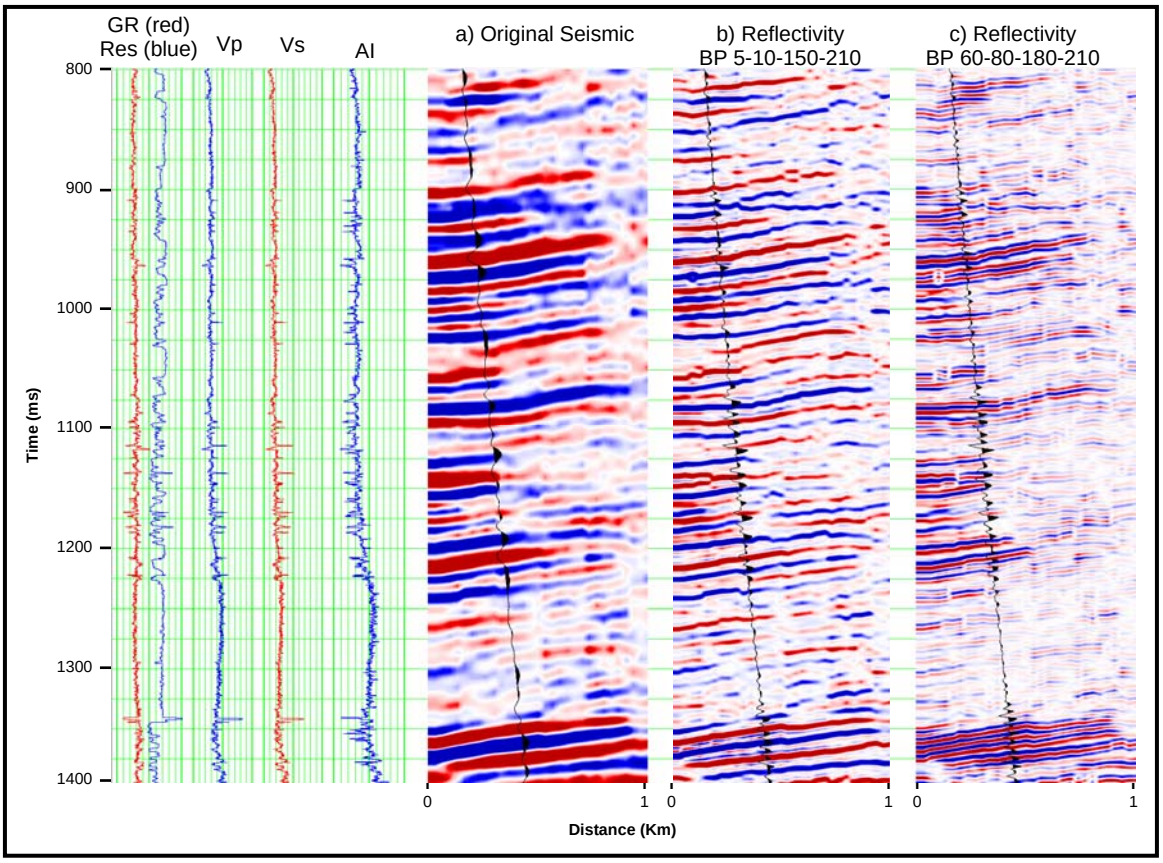

Figure 48: Comparison of 3 different seismic sections and their correspondent synthetic seismograms. The original seismic section without any filter (a), a reflectivity band limited 5-10-150-210 section (b) and a high pass (60-80-180-210) reflectivity section (c).

The last panel (Figure 48c and 49c) shows a section of the reflectivity inversion with a high pass filter (BP 60-80-180-210), with frequency content above the frequency band of the original seismic data (Figure 46). The same frequency band filter was also used to recreate a wavelet and convolve it with the reflectivity series. Again, the tie results are compared in the vicinity of the well showing a correlation of 0.26 in Figure 48c and 0.35 in Figure 49c.

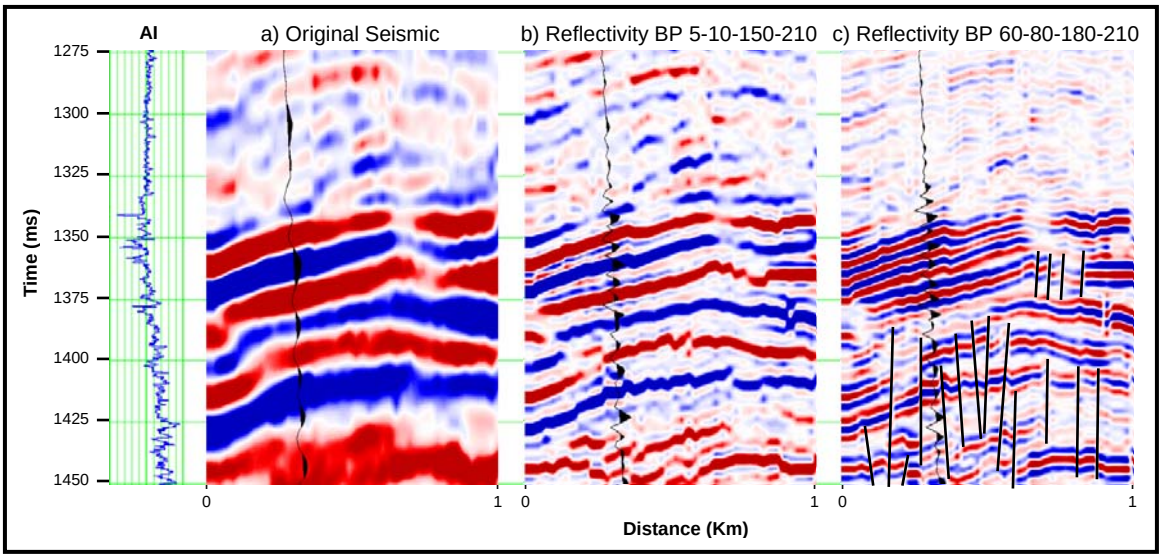

Figure 49: Closer look at the base of the synthetic tie on figure 48. The original seismic section (a), a reflectivity band limited 5-10-150-210 section (b) and a high pass (60-80-180-210) reflectivity section (c). Black lines show small faults not obvious in the original amplitude data.

Because the data used are beyond the original data bandwidth, the spectral inversion process is still recovering information that was not available in the original data. The geology looks consistent between the volumes and the increase in resolution is noticeable, where a preliminary interpretation on the reflectivity volumes shows several faults not obvious in the original seismic data (black lines in Figure 49c).

The analysis showed that the correlations of the synthetic seismograms with the reflectivity volumes are lower compared to the original seismic. This is mainly due to the fact that higher frequency content in the reflectivity volumes introduces greater variability in the velocity. Additionally, the synthetic seismograms were not squeezed or stretched in order to favor the correlation coefficients. Other explanations for these lower correlation coefficients could be: 1) the wavelets applied to the synthetics were not

extracted from the seismic and were instead generated using a band-pass filter, or 2) noise increases along with frequency content.

The reflectivity inversion provides information about thickness and faulting that could not be seen before due to the overprint of the wavelet. When referring to thickness, a pseudo-impedance volume can also be calculated using the reflectivity inversion volume as input and applying a -90 degree phase rotation to it. Then, this relative impedance will provide the thickness variation of the sand bodies. Figure 50 shows 3 seismic sections from the original, reflectivity inversion, and pseudo-impedance (inversion) seismic volume respectively. An increase in impedance is a peak (blue) and a decrease in impedance is a trough (red).

An induction log was used for the interpretation, as the GR log does not help to distinguish between sand and shale in this field due to the lithologic complexity and composition. The peak frequency of the original seismic data is approximately 18 Hz, and the velocity obtained from the P-wave log is on average 2800 m/s for the Sterling Formation. The wavelength of the seismic wavelet is given by the division of the velocity and frequency, which is 155 m, and the limit of resolution will be 39 m. Because the seismic is in the time domain, layers below 28 ms tuning thickness are not resolved with the original seismic data.

It can be observed that the gas sands show higher impedances than shales (Figures 50 and Apendix C.1). The boundaries at the top and base of the main gas sand are not

distinguished in the original seismic data (below tuning, 12 ms time thickness equivalent to 17 m), whereas in the reflectivity and impedance sections the main gas sand is resolved. Notice that the pseudo impedance and reflectivity inversion fail to capture the fining upward sand below the high impedance gas sand, while the reflectivity is able to capture just its base.

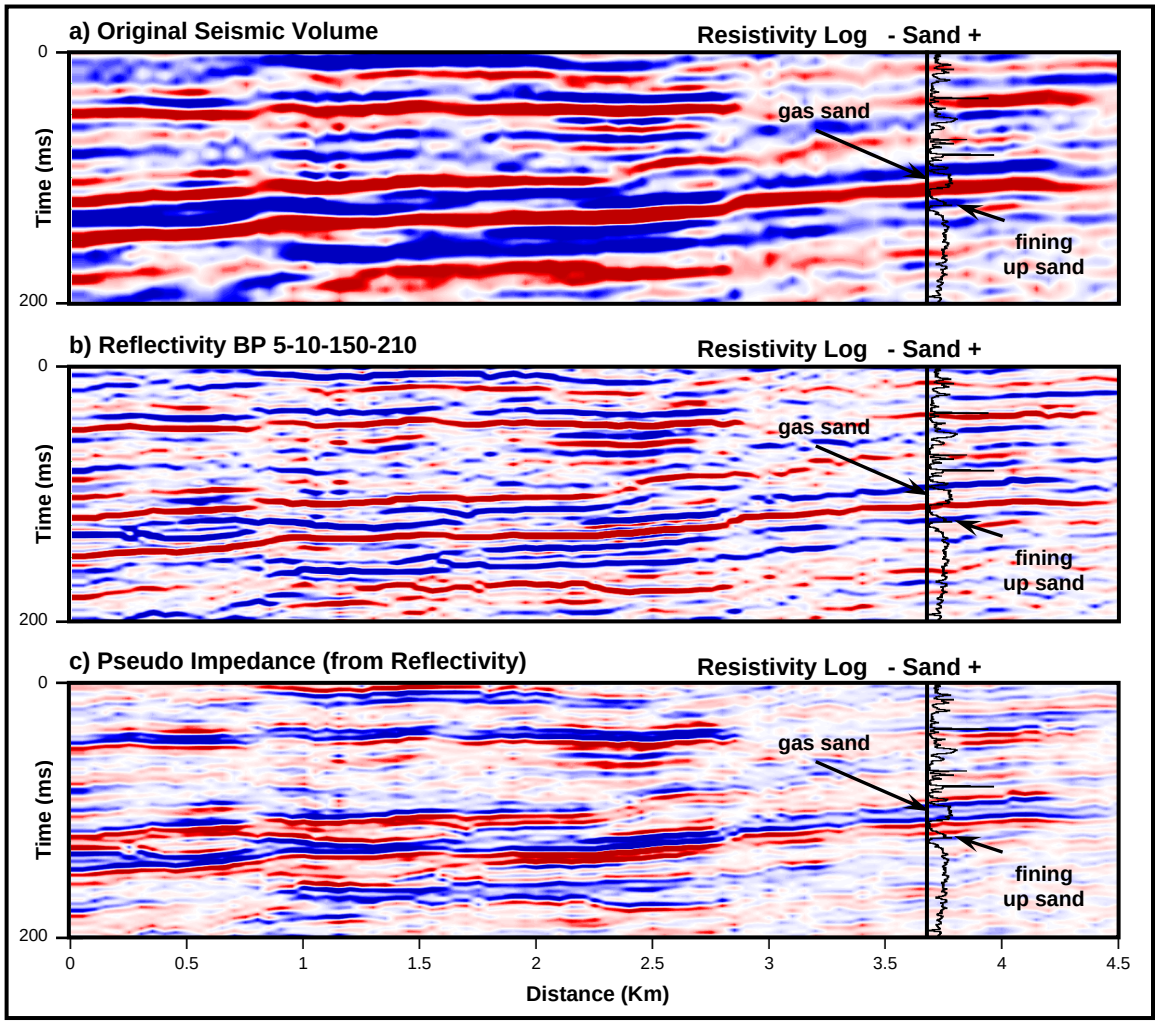

Figure 50: Comparison of the original seismic (a), the reflectivity band limited 5-10-150-210 (b) and pseudo-impedance sections (c) with an induction log. High impedance gas sand (12ms time thickness) is resolved by the inversion on the reflectivity and impedance volumes. The tuning thickness is 28 ms for the original seismic data. An increase in impedance is a peak (blue) and a decrease in impedance is a trough (red).

5.4 Stratigraphic Interpretation

The reflectivity volume obtained from the spectral inversion improves the vertical resolution and reveals the geology masked by the wavelet. The inversion allows a more precise stratigraphic and structural interpretation. A comparison between the original seismic and inverted reflectivity sections (Figure 51 and 52) shows that when the wavelet is removed, reflections are better highlighted by the reflectivity data. Furthermore, their lateral continuity is enhanced by showing details that could not be interpreted using the conventional seismic data.

Picking the stronger events or reflections on both seismic sections from figure 51 and comparing them in figure 52, shows that the quantity of information obtained from the inverted data is more detailed. When both interpretations are superimposed (Figure 52c)**,** the events extracted from the inversion may be related to stratigraphic patterns (see inside circles in figure 52c). These patterns could correspond to amalgamated sequences of bar deposits shown in the GPR example (Figure 38). However, these stratigraphic patterns could be also related to noise due to the expansion of the frequency band. The uncertainty could be reduced with greater well control. Using an oilfield with many wells and a defined geological model could be recommended for future work.

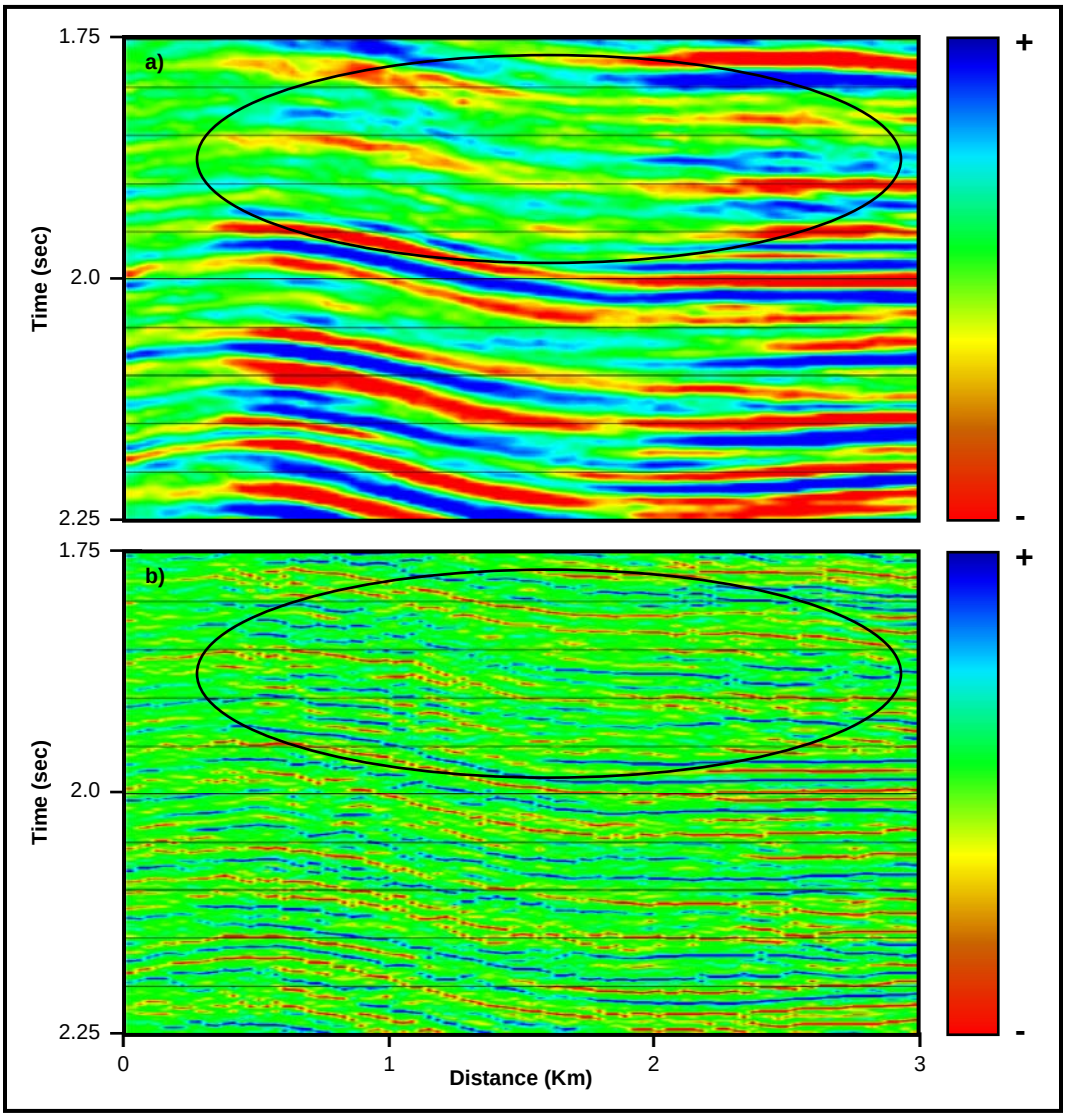

Figure 51: Comparison of the original seismic (a) and inverted data (b). Stratigraphic patterns related to the geology are highlighted within the reflectivity that could not been seen on the conventional-stack seismic data. Peaks are blue and troughs red.

The description of braided systems by Bridge (2006) consist mainly of very thin deposits (<1 to 3m). Improvement in resolution might image channel belts rather than individual channels or bars, which are difficult to observe even with the highest resolution seismic data. Taking into consideration that the inversion process is made

trace-by-trace, and no lateral continuity was assumed, the reflection coefficients from the inversion might show a better representation of the stratigraphy.

The concept of constructive and destructive interference can be clearly seen in figure 53. The stratigrapgy seems to be essentially simple and flat on the original seismic data (Figure 53a). Some reflections interfere constructively, while others disappear due to destructive interference.

The solution obtained from the spectral inversion (Figure 53b) preserves the lateral continuity of the stratigraphy previously hidden in the original seismic data (wavelet filter), and now all the events are clearly separated into different reflection coefficients (figure 53b). Not only can reflections be interpreted along the whole section, but some structural features can also be seen. Small faults or fractures could not be detected in the original seismic sections (Figure 53c), but now they can be identified on the inverted reflectivity seismic section (Figure 53b).

Figure 52: Comparison of interpretations made on the original seismic (a) and inverted data (b) from figure 51. c) When both interpretations are superimposed (red and blue colors represent the interpretation made in the original seismic and reflectivity data respectively), more stratigraphic patterns are visible in the inverted data that could correspond to amalgamated sequences of bar deposits (10 ms ~ 14 m thick).

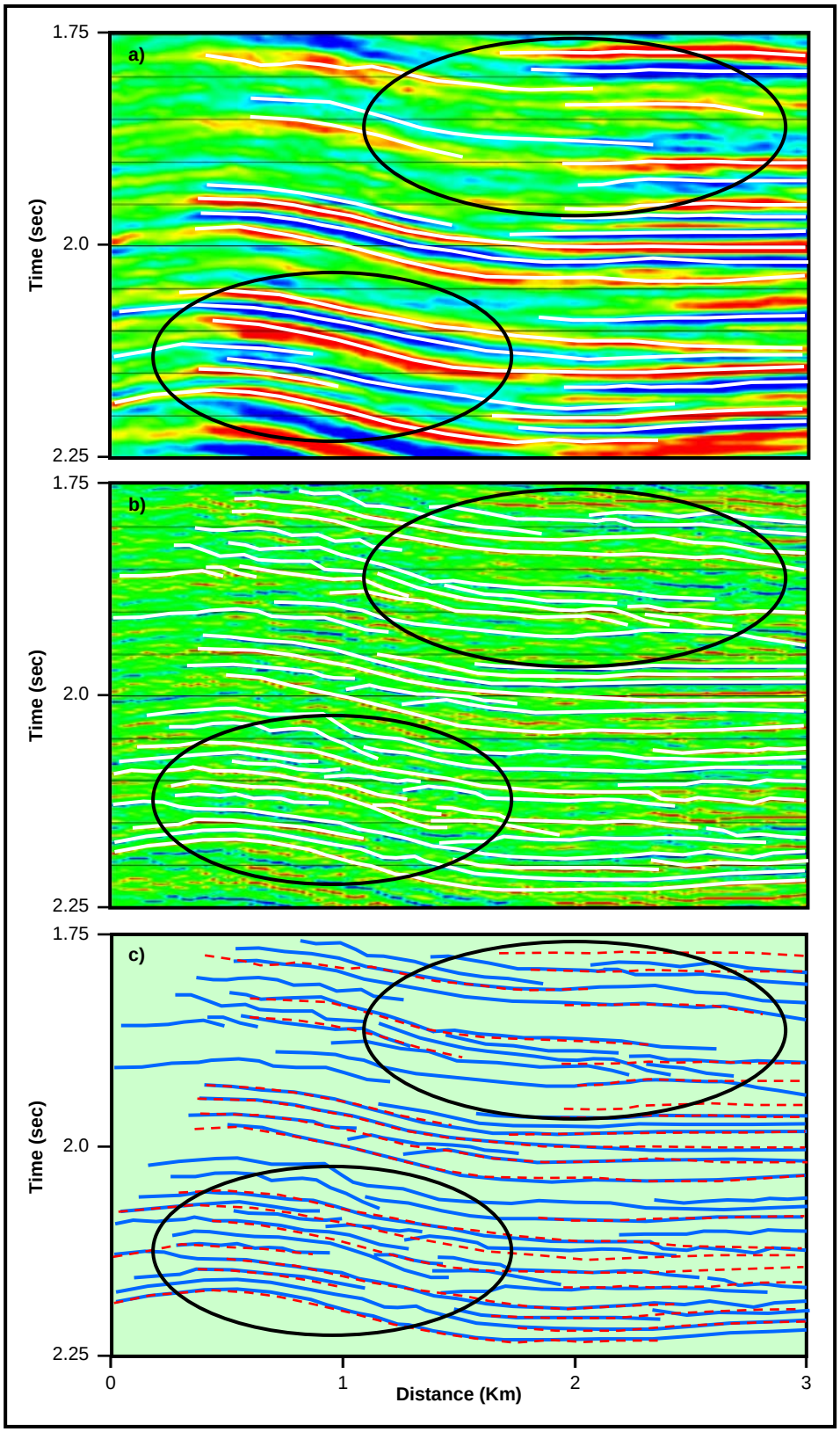
a)
b)
c)
1.75
2.0
2.25
Time (sec)
0
1
2
3
Distance (Km)

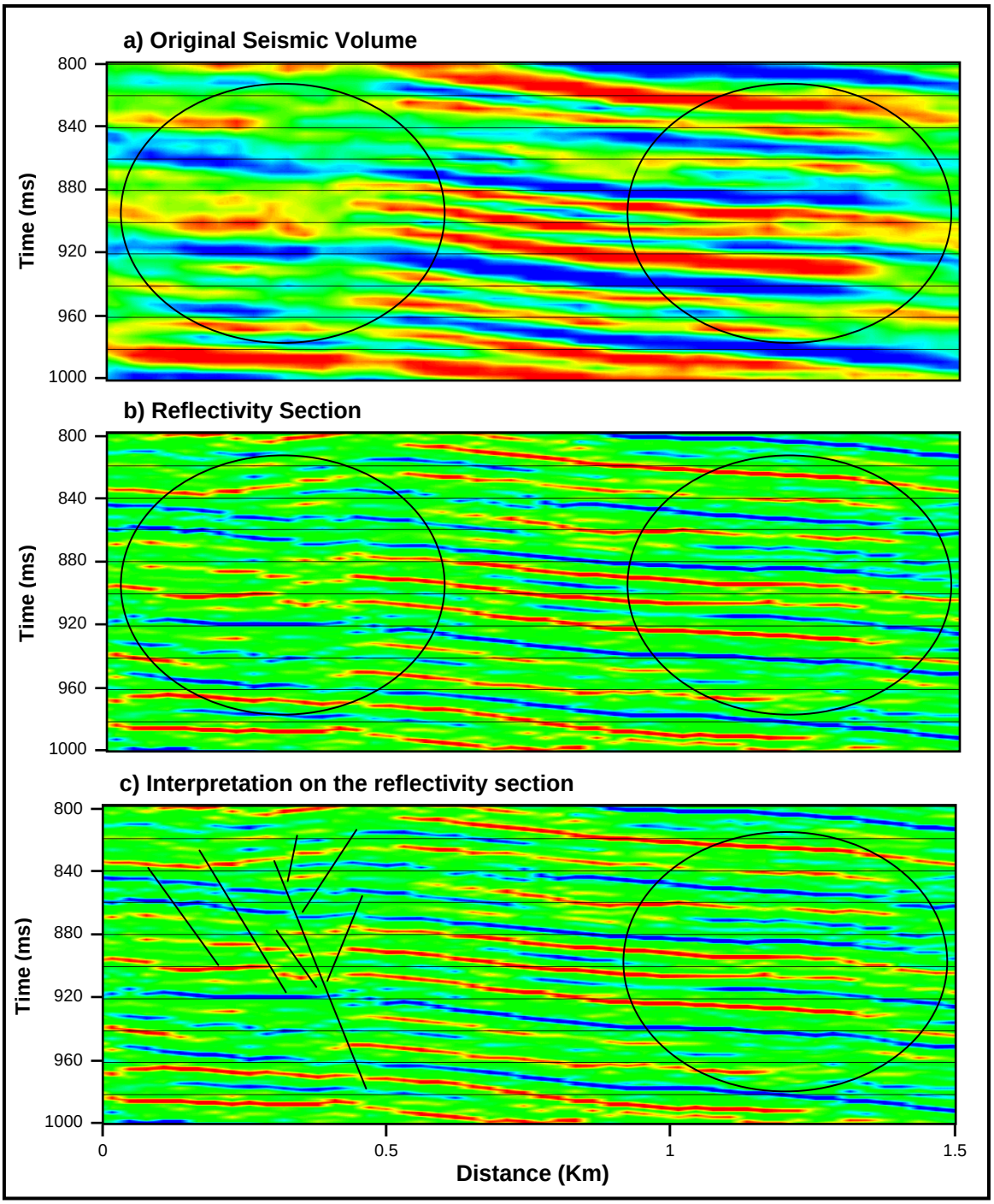

Figure 53: The comparison between images clearly shows the concept of constructive and destructive interference on the full stack seismic section (a). The inverted data (b) not only preserves and improves the lateral continuity of the stratigraphy, but separates and highlights events that could not been observed before. Some small faults or fractures can also be interpreted.

5.5 Spectral Decomposition and Inversion Visualization

The use of different seismic attributes for stratigraphic interpretation and 3D visualization helps the geoscientist to characterize and understand the subsurface. In this case, the spectral decomposition MPD algorithm was applied to the full stack seismic data, creating common frequency volumes from 0 Hz to 80 Hz. The peak-amplitude volume was calculated and used for attribute extractions. In addition to the frequency volumes, the original seismic amplitude data, the reflectivity, and pseudo-impedance volumes produced from the inversion were also used, not only for horizon interpretation, but also for attribute extractions. Several horizons were interpreted for the Sterling A8, B2, and C1 sand tops as well as the top of the upper Beluga Formation.

An RMS amplitude extraction was performed along the Sterling A8 horizon, using a 10 ms time window for the full seismic stack, pseudo-impedance, and peak-amplitude (maximum amplitude value at every peak frequency) volumes (Figure 54a, 54b, and 54c). The visualization enhancement obtained is notable compared with the original seismic data. Some braided channel patterns, braid-bar assemblages and flood plains, shown by colors in figure 54d, were extracted from the impedance and peak-amplitude volumes. The deposition direction observed is NE-SW, corresponding to the regional geology described previously. Some small braided channel shapes can also be recognized between small braid bars within channel belt, especially in the peak amplitude volume. Although, the image quality is affected by the Kenai River, there is not bias on the interpretation produced, because its actual fairway goes from SE to NW.

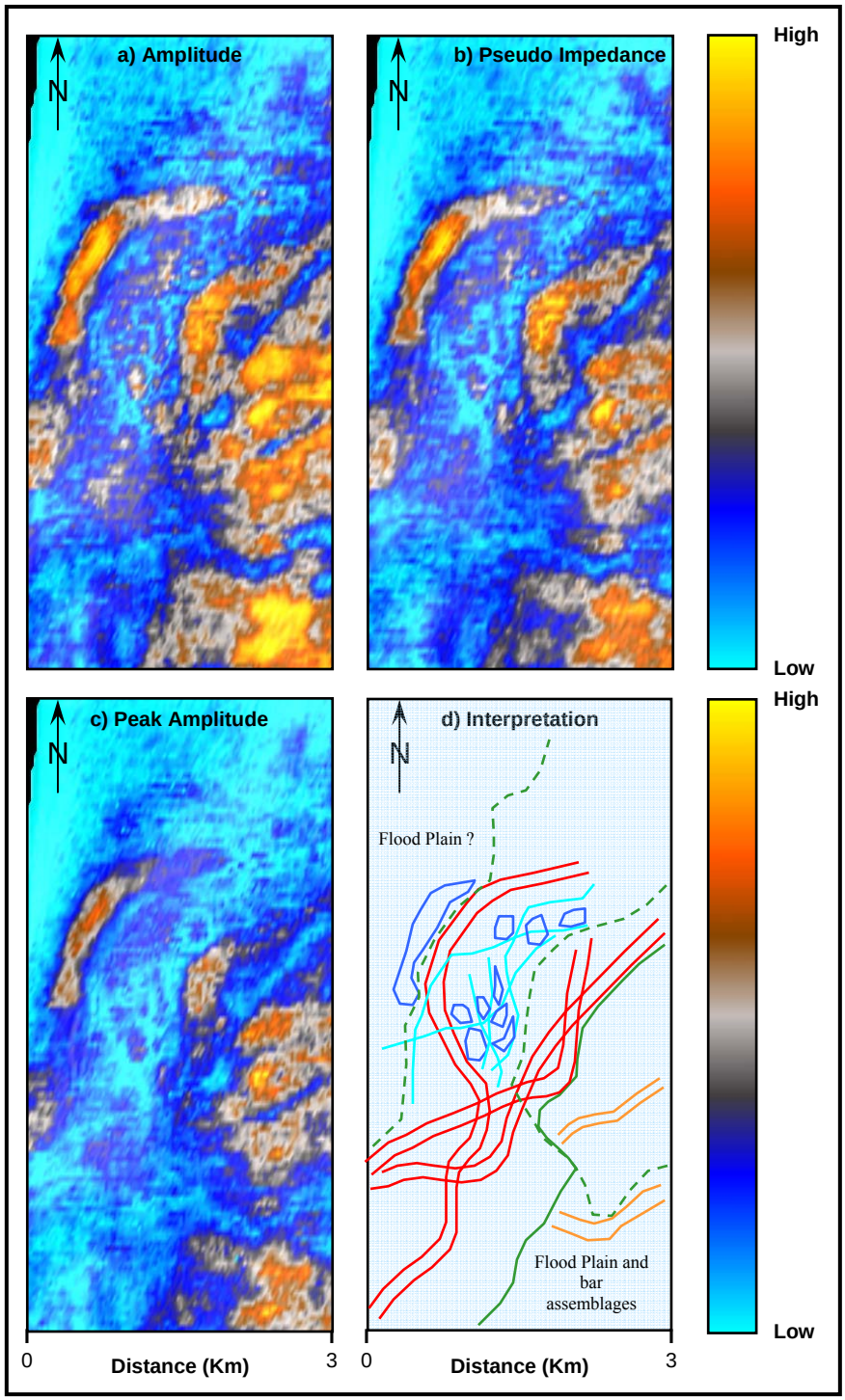

Figure 54: 10 ms time window RMS amplitude extractions on the Sterling A8 horizon comparing the full stack seismic (a), pseudo-impedance (b) and peak-amplitude volumes (c). Interpretation, extracted from the peak-amplitude and pseudo-impedance attributes (d), show some channels patterns (red and cyan), bar assemblages (blue), and flood plain (green) composed by some channels (orange) and bar assemblages.

On a different horizon, the B-2 sand of the Sterling Formation, an RMS amplitude extraction on a 10 ms time window was calculated using the original amplitude seismic section and reflectivity volume with a band-pass filter defined by the 5-10-80-125 frequencies. In this case, the reflectivity used has an 80 to 125 Hz band that the original data did not. The amplitude volume shows a channel feature towards the south, still preserving the same regional deposition direction. The rest of the extraction shows a group of massive bright bodies that could be assemblages of bars (Figure 55a). On the other hand, the band-pass reflectivity volume shows a crisper image not only of the same channel, but also another channel highlighted to the west, as well as some features that appear to be channels and bars in the middle of the channel belt (Figure 55b). The peak-amplitude and impedance RMS extractions can be seen in Appendix C.3, but the best results were obtained when interpreting different frequency maps from figure 56.

Using a 20 ms time window, an RMS amplitude extraction was made on the same B-2 horizon using the 8 Hz (Figure 56a), 20 Hz (Figure 56b), 32 Hz (Figure 56c), 44 Hz (Figure 56d), and 56 Hz (Figure 56e) frequency volumes. The interpretation extracted from each volume (Figure 56f) shows different deposits of the interpreted braided system. Figure 56f shows thick bars (black), thinner bar assemblages (blue), two different sizes of channels (red and cyan), and flood plain (green) with some small channels (orange). It can also be concluded that the point bars, generated probably by lateral accretion, are the thickest deposits in the channel belt and are better illuminated at low frequencies (8 and 20 Hz). However, using higher frequency volumes, thin deposits are inferred, like channels and bars complexes. Then, using and merging the interpretation

from each volume, a better characterization of the depositional systems and reservoirs can be achieved. The interpretation could correspond with the analog case described of the Sagavanirktok River, northern Alaska, by Bridge (2006) in figure 37.

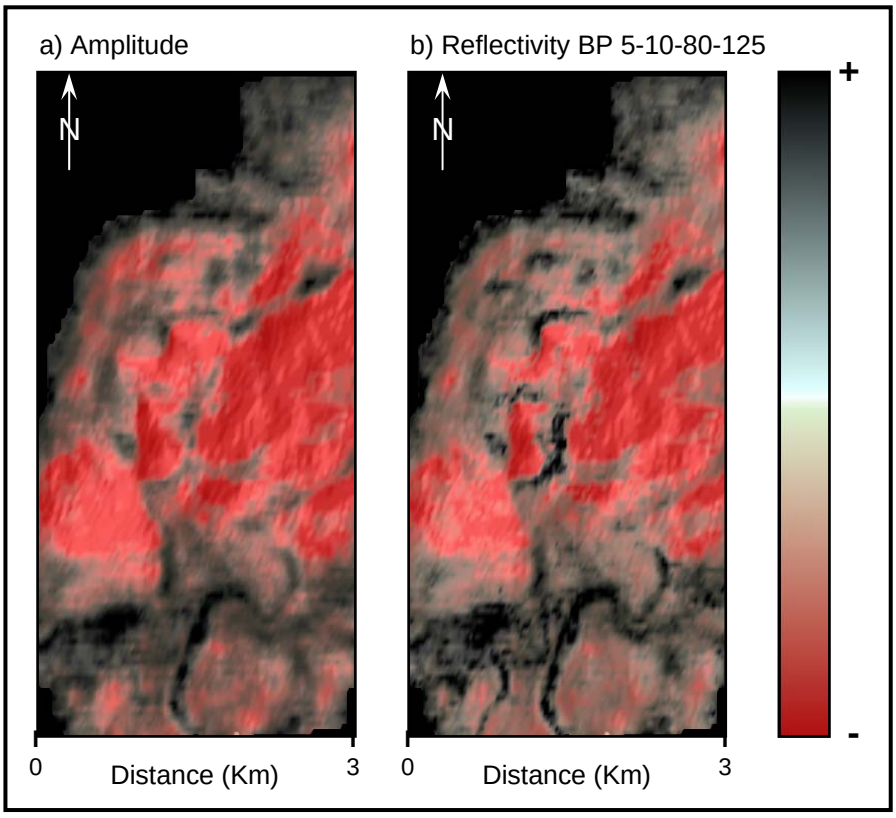

Figure 55: Comparison between RMS amplitude extractions along the Sterling B2 horizon on a 10 ms time window for the full stack seismic (a) and a reflectivity with a band-pass filter (BP 5-10-80-125). Notice the visualization enhancement for some channels patterns to the south and center of the field.

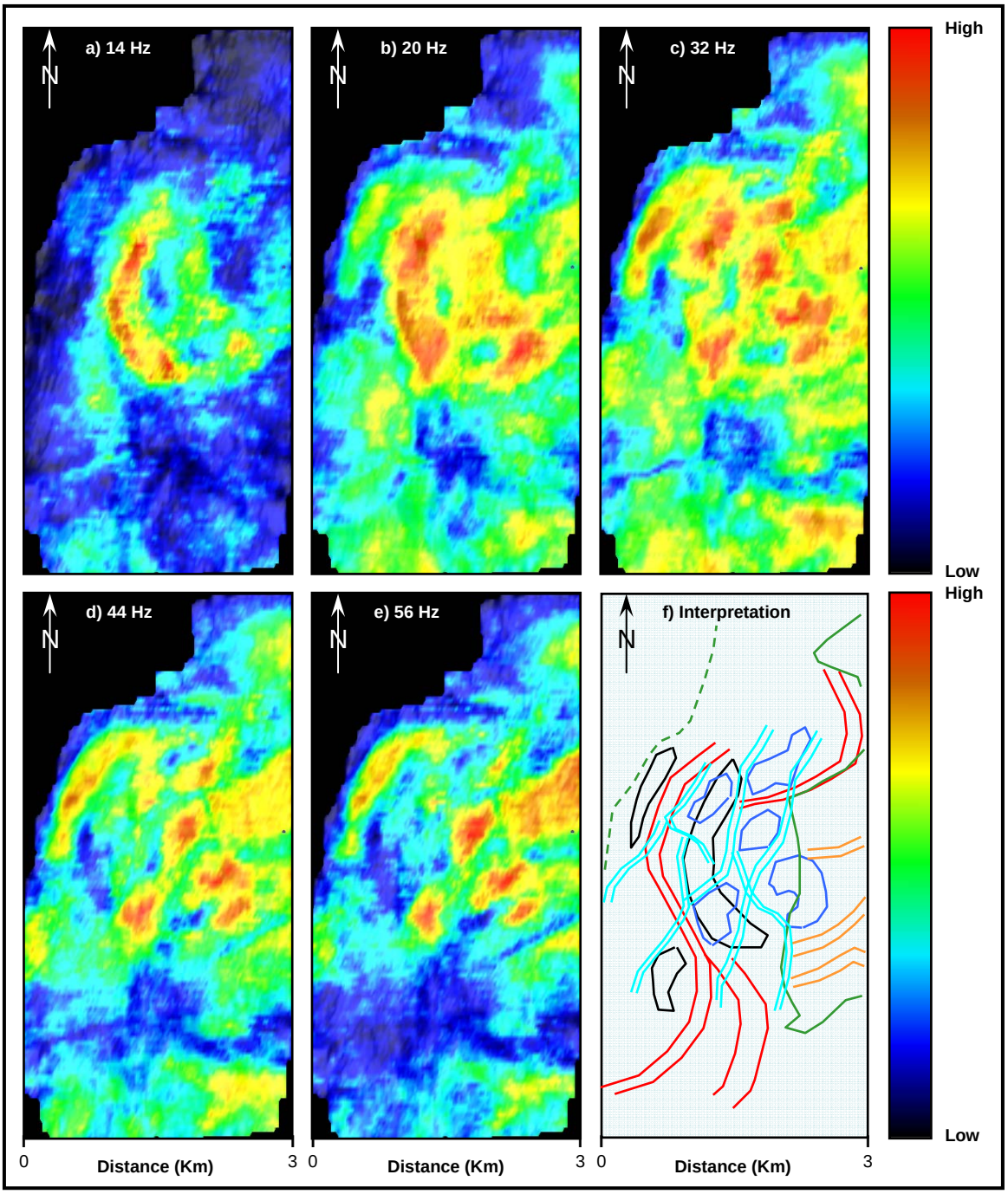

Figure 56: 20 ms time window RMS amplitude extraction on horizon B-2, using the 8(a), 20(b), 32(c), 44(d) and 56(e) Hz frequency volumes. Interpretation extracted from each volume shows different deposits (f) of the braided system interpreted. Thick bars (black), thinner bar assemblages (blue), two different channel sizes (red and cyan) and that could be interpreted as flood plain (green and dash green) or bar assemblages with some small channels (orange). This interpretation is similar to the analog case described by Bridge (2006) of the Sagavanirktok River, northern Alaska.

5.6 Low-Frequency Shadow Reservoir Detection

Part of the interpretation process was to scan all the frequency volumes using seismic sections and map views. Several observations were made to identify amplitude anomalies at different frequencies to determine which could be related to the presence of hydrocarbons.

In this study, a low-frequency shadow was identified and associated with the C-1 Sterling Formation gas sand (confirmed by the single producing well), where the average thickness is around 18 m. This shadow could be related to abnormally high attenuation in the gas reservoir. Because the total producing zone (4 sands in the well) is approximately 46 m thick, it is possible to explain such attenuation, since the zone is thick enough to produce the effect. Two seismic sections (Figure 57a and 57b) showing amplitude and their respective common frequencies for 11 Hz (Figure 57c and 57d), show two abnormally high energy zones beneath two different reservoirs. The deepest one is the one that corresponds to the C-1 gas sand. On higher frequency sections (32 Hz) the energy disappears completely (Figures 57e and 57f).

An RMS amplitude extraction was generated for both frequency volumes using the C-1 horizon in two different time windows, 60 ms within the reservoir and 100 ms below the reservoir (Figure 58). The reservoir is highlighted by a black line. The maps show how on the 11 Hz common frequency maps there is not much energy above the reservoir (Figure 58a) but there is clear shadow below it (Figure 58b). The opposite effect

occurs when the 32 Hz frequency maps are observed. The reservoir is highlighted in the time window above the reservoir, while the energy disappears in the amplitude extraction below the reservoir.

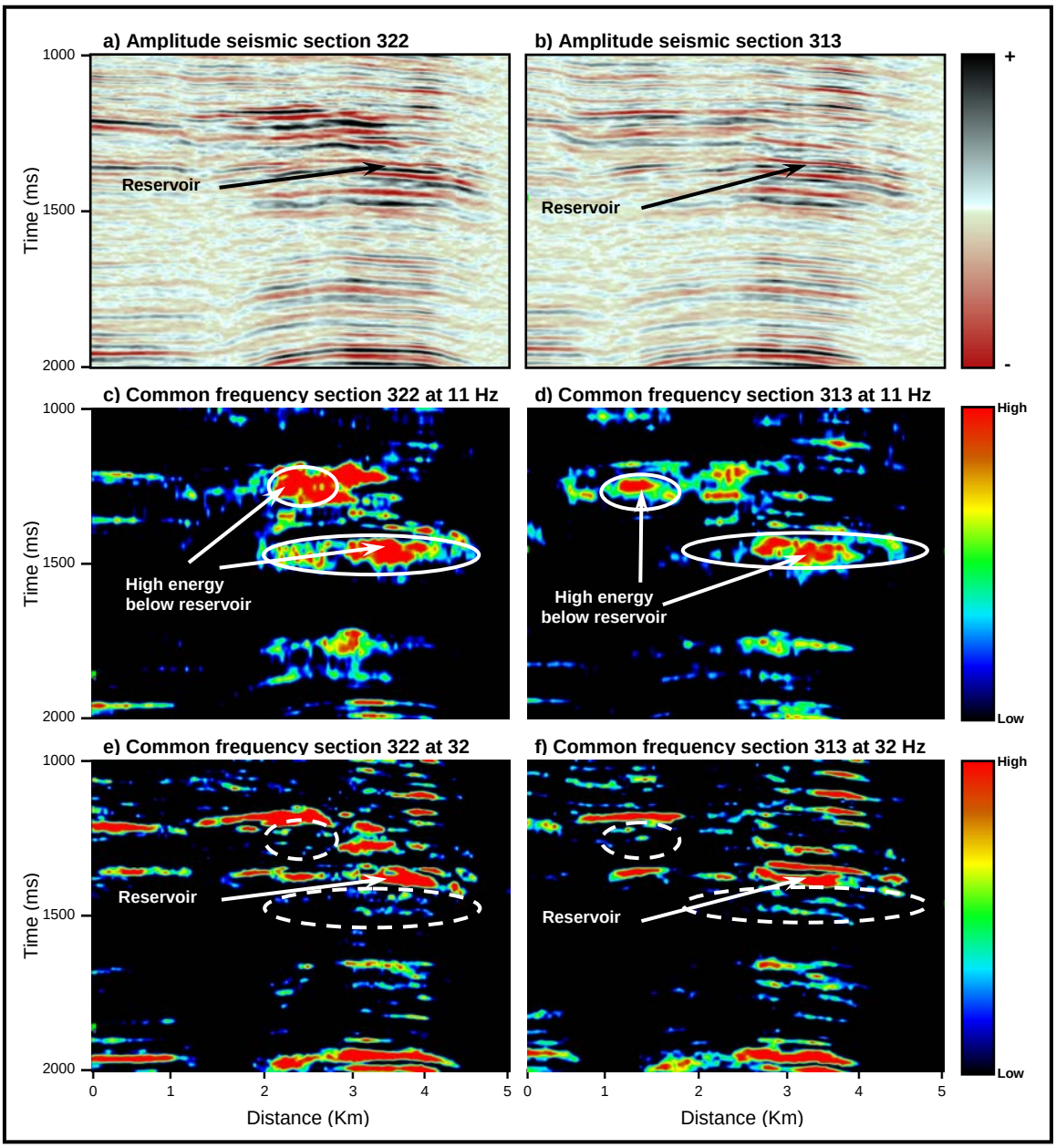

Figure 57: Two seismic sections (a, b) showing amplitude and their respective common frequencies for 11 Hz (c, d) and 32 Hz (e, f).The low-frequency shadow zones, just beneath the reservoir, are the strongest events on the sections, marked within a white ellipse (c, d). On the other hand, at 32 Hz (e, f) the reservoir is illuminated and the energy disappears.

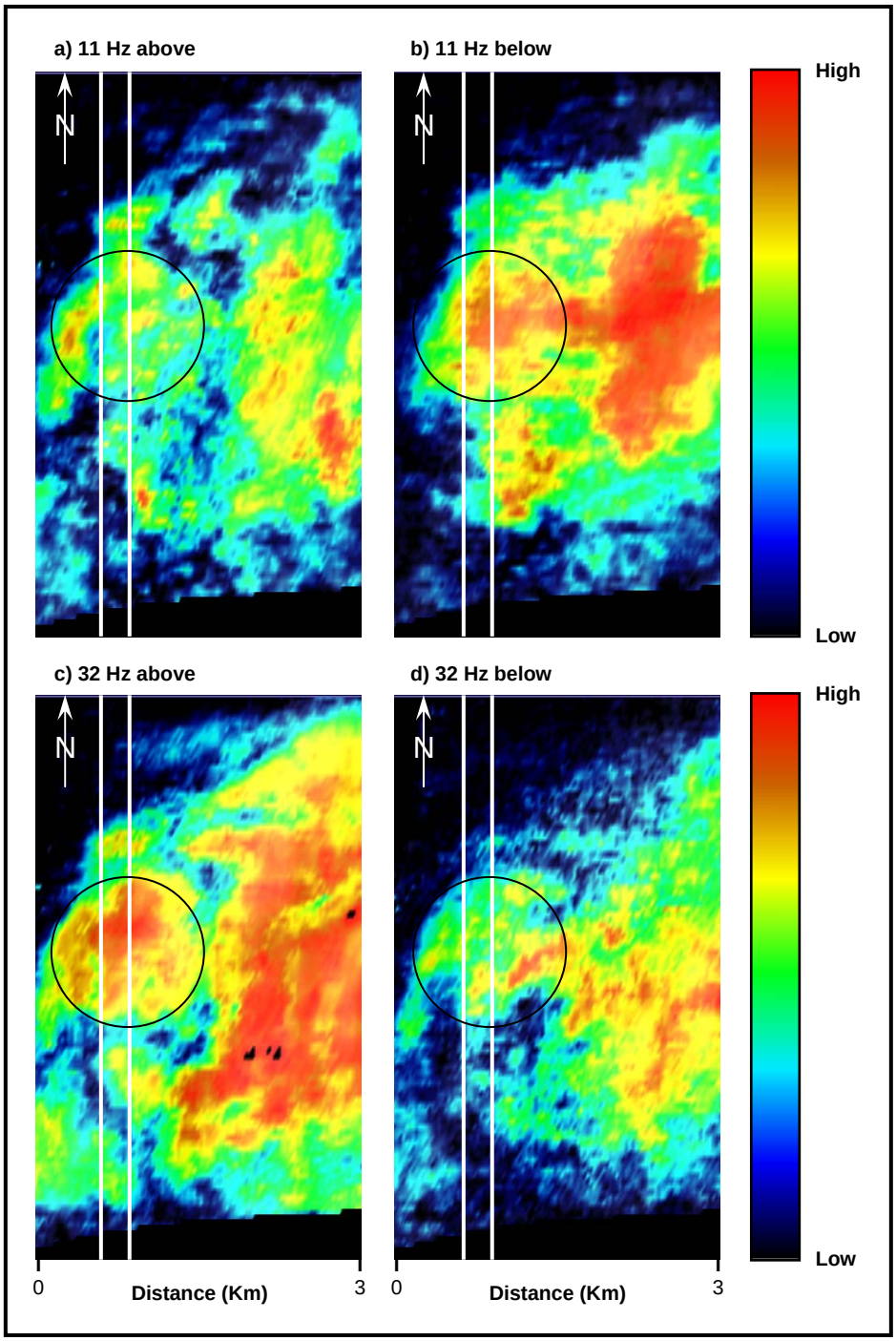

Figure 58: Amplitude extraction maps from the 11 Hz (a, b) and 32 Hz (c, d) common frequency volumes. The extraction was performed in a 60 ms time window within (a, c) and 100 ms time window below (b, d) the reservoir respectively. The black circle identifies the reservoir location. At 11 Hz the energy below the reservoir is stronger than above the reservoir. On the other hand, at 32 Hz just the opposite occurs. White lines show the position of the sections from figure 57.

The MPD spectral decomposition algorithm was applied to this dataset and to the synthetic data; both show better vertical and spectral resolution. Analyzing seismic data in the frequency domain provides better evidence of hydrocarbons than full-stack seismic data.

The Alaska example shows that the shadows have more energy than the reservoir reflections, and that at a certain frequency the reservoir is more anomalous than the background. This could be related to the thickness, and/or presence of fluid.

This shadow phenomenon should not be related to simple attenuation, because all frequencies, especially higher, are not being attenuated. In contrast, low-frequency energy is boosted (Castagna, et al., 2003). The low-frequency shadow could be related to one of the mechanisms described in Ebrom (2004). Such mechanisms are related to complex acquisition parameters or data processing (such as incorrect NMO correction, or stretch of the far offset). Unfortunately, the gathers were not available for this project, but it would be valuable to perform a future study relating frequency and offset.

6. CONCLUSIONS

6.1 Summary

As shown in synthetic models and in real data, the theory behind spectral decomposition and inversion are novel techniques that can be applied to seismic data revealing details about the geology and rock property that are suppressed by the wavelet.

The wavelet extraction process is probably the most important process in seismic inversion. It was demonstrated on synthetic models that the incorrect characterization of the wavelet can lead to incorrect results. All inversion techniques should allow accurate extraction of time and spatial variant wavelets, similar to the reflectivity inversion process carried out in this study.

The spectral inversion analyses obtained from the synthetic wedge models demonstrate that the frequency bandwidth of the original seismic data does not seem to affect the inversion results for high S/N ratio cases. Nevertheless, noise in low-frequency content data will partially affect the inversion, as the need for expanding the original frequency bandwidth also boosts the noise.

The presence of noise is the main problem and can limit the results of any seismic inversion. For that reason, noise suppression during acquisition and processing will establish the resolution limits more than any other seismic parameter.

The results from the Alaska dataset show that the spectral inversion process boosts the higher frequencies, but also boosts part of the noise already present in the data. The reflectivity data were more stable and superior in vertical resolution than the original seismic data, as indicated by well log comparisons, where thin sands below tuning thickness were resolved. The geology is better represented by the reflection coefficients; therefore geological models created from the inversion are superior in defining stratigraphic patterns and delineating small faults.

The frequency attributes (peak-amplitude and common-frequency volumes) and inversion obtained and interpreted in the Alaska dataset, highlighted geomorphologic elements (channels, bars, and floodplains) that in most cases could not be interpreted using the original seismic data. In spite of the fact that depositional systems, like this braided systems, are difficult to illuminate and visualize in seismic data, especially when the data quality is poor, the attribute integration and careful interpretation improve the understanding of the oil field. The main reason is that there is information related to lateral layer thickness variation, temporal thickness, and geomorphology that can be extracted from the frequency domain, facilitating the detection of geological discontinuities and/or reservoir delineation.

Using a spectral decomposition algorithm that offers accurate and stable spectral and time resolution recovers more information from the frequency domain than the widely used DFT or CWT methods. Using spectral decomposition or other seismic

attributes, does not guarantee visualization of geology or rock properties, because they are highly dependent on data quality, and on the algorithm used.

6.2 Future Work

Since the response to hydrocarbon in the frequency domain is not perfectly understood yet, more studies are needed in this direction. Working with gathers for different AVO scenarios and for different time thicknesses could lead to a better understanding of this response. The low-frequency shadows, can help delineating the reservoir, but integration with synthetic models will lead to better understand the cause of such events.

Using a high quality dataset, where the subsurface geology is well known, could be a good verification test for the spectral-inversion process. At the same time, the application in simultaneous elastic inversion could also lead to enhanced reservoir characterization and understanding lithology and fluid behavior.

REFERENCES

Bridge, J., 2006, Fluvial facies models: Recent developments, in: Posamentier, H. and Walker, R. (eds.), Facies Models Revisited, SEPM Special Publication No. 84, 83-168.

Brimberry, D. L., P.S. Gardner, M.L. McCullough, and S.E. Trudell, 2001, Introduction to Tertiary tectonics and sedimentation in the Cook Inlet Basin, in: 2001 Guide to the petroleum, geology, and shallow gas potential of the Kenai Peninsula, Alaska, A field trip guidebook compiled by Dallegge, T., during the Alaska Coalbed and Shallow Gas Resources workshop sponsored by the West Coast PTTC, Alaska Department of Natural Resources, and U.S. Geological Survey held on April 30 – May 1, 2001, p. 20-28.

Brown, A., 1999, Interpretation of Three-dimensional Seismic Data: SEG/AAPG, SEG Investigations in Geophysics #9, 6th Edition, 560 pp.

Burnett, M., J. P. Castagna, E. Méndez Hernández, G. Ziga Rodríguez, L. Figón García, J. Martínez Vázquez, M. Téllez Avilés, and R. Vila Villaseñor, 2003, Application of spectral decomposition to gas basins in Mexico: The Leading Edge, 22, 1130-1134.

Castagna, J. P., S. Sun, and R.W. Siegfried, 2003, Instantaneous spectral analysis: Detection of low-frequency shadows associated with hydrocarbons: The Leading Edge, 22, 120–127.

Castagna, J. P., 2005, Spectral decomposition and high-resolution reflectivity inversion: Presented at CSEG National Convention, ‹wildhorse.insinc.com/cseg/castagna/›.

Castagna, J. P., and S. Sun, 2006, Comparison of spectral decomposition methods: First Break, EAGE, 24, 75-79.

Chakraborty, A., and D. Okaya, 1995, Frequency-time decomposition of seismic data using wavelet-based methods: Geophysics, 60, 1906-1916.

Chopra, S., J. Castagna, and O. Portniaguine (2006), Seismic resolution and thin-bed reflectivity inversion: CSEG Recorder, 31, 19-25.

Ebrom, D., 2004, The low-frequency gas shadow on seismic sections: The Leading Edge, 23, 772 p.

Fahmy, W., G. Matteucci, D. Butters, J. Zhang, and J. Castagna, 2005, Successful application of spectral decomposition technology toward drilling of a key offshore development well: 75th Annual International Meeting, SEG, Expanded Abstracts, 24, 262-265.

Gridley, J., and G. Partyka, 1997, Processing and interpretational aspects of spectral decomposition: SEG Expanded Abstracts, 16, 1055-1058.

Hayes, J. B., J. C. Harms, and T. Wilson, 1976, Contrasts between braided and meandering stream deposits, Beluga and Sterling Formations (Tertiary), Cook Inlet, Alaska, in: Miller, T.P. (ed.), Recent and Ancient Sedimentary Environments in Alaska, Proceedings of the Alaska Geological Society Symposium held April 2-4, 1975, at Anchorage, Alaska, p. J1-J27.

Hernandez, D., and J. Castagna, 2004, Stratigraphic detection and hydrocarbon detection in offshore Gulf of Mexico, Miocene sandstone reservoirs using spectral

Decomposition: 74th Annual International Meeting, SEG, Expanded Abstracts, 23, 533-536.
Kallweit, R. S., and L. C.Wood, 1982, The limits of resolution of zero-phase wavelets: Geophysics, 47, 1035–1046.
Mallat, S., and Z. Zhang, 1993, Matching pursuit with time-frequency dictionaries: IEEE Transactions on Signal Processing, 41, 3397– 3415.
Marfurt, K. J., and R. L. Kirlin, 2001, Narrow-band spectral analysis and thin bed tuning: Geophysics, 66, 1274-1283.
Odebeatu, E., J. Zhang, M. Chapman, E. Liu, and X. Li, 2006, Application of spectral decomposition to detection of dispersion anomalies associated with gas saturation: The Leading Edge, 25, 206-210.
Partyka, G., J. Gridley, and J. Lopez, 1999, Interpretational applications of spectral decomposition in reservoir characterization: The Leading Edge, 18, 353–360.
Portniaguine, O., and J. P. Castagna, 2005, Spectral inversion: Lessons from modeling and Boonesville case study: 75th Annual International Meeting, SEG, Expanded Abstracts, 24, 1638-1641.
Puryear, C. I., 2006, Modeling and application of spectral inversion for determination of layer properties: M.S. thesis, University of Houston, 56 pp.
Puryear, C., and J. P. Castagna, 2008, Layer-thickness determination and stratigraphic interpretation using spectral inversion: Theory and application: Geophysics, 73, R37-R48.
Rauch-Davies, M., and M. Graham, 2006, Using spectral decomposition and coherence for reservoir delineation and fluid prediction in extensively explored region: 76th Annual International Meeting, SEG, Expanded Abstracts, 25, 690-694.
Sinha, S., P. Routh, P. Anno, and J. P. Castagna, 2005, Spectral decomposition of seismic data with continuous-wavelet transform: Geophysics, 70, P19-P25.
Swenson, R., 2001, Introduction to Tertiary tectonics and sedimentation in the Cook Inlet Basin, in: 2001 Guide to the petroleum, geology, and shallow gas potential of the Kenai Peninsula, Alaska, A field trip guidebook compiled by Dallegge, T., during the Alaska Coalbed and Shallow Gas Resources workshop sponsored by the West Coast PTTC, Alaska Department of Natural Resources, and U.S. Geological Survey held on April 30 – May 1, 2001, p. 10-19.
Tirado, S., 2004, Sand thickness estimation using spectral decomposition: M.S. thesis, University of Oklahoma, 63 pp.
Widess, M. B., 1973, How thin is a thin bed?: Geophysics, 38, 1176-1180.

APPENDIX A

Synthetic seismograms generated for three different wells using Ricker wavelets with predominant frequencies of 35 and 25 Hz. The synthetics were created for the upper section (Sterling Formation) and middle section (Beluga Formation and deeper rocks).

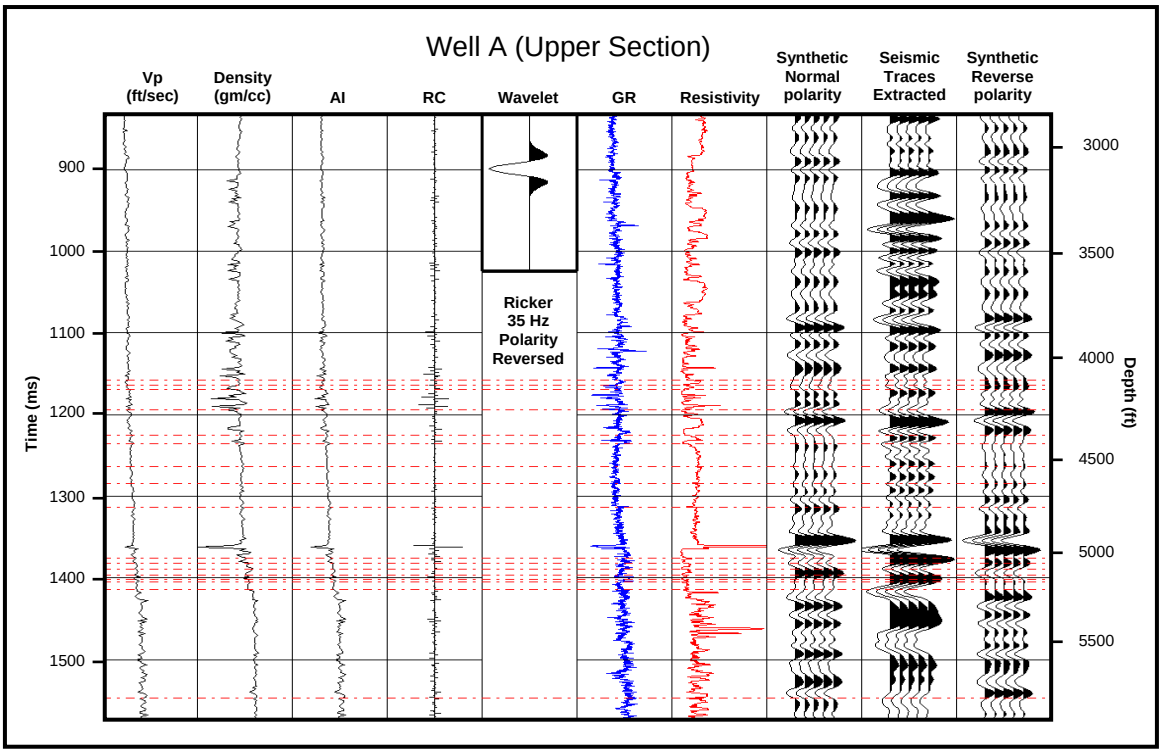

Figure A.1: Synthetic seismogram for the upper section of Well A using a Ricker wavelet of 35 Hz. The tie is good. Notice the reverse polarity of the wavelet, demonstrating that the seismic needed a phase rotation of -180 degrees.

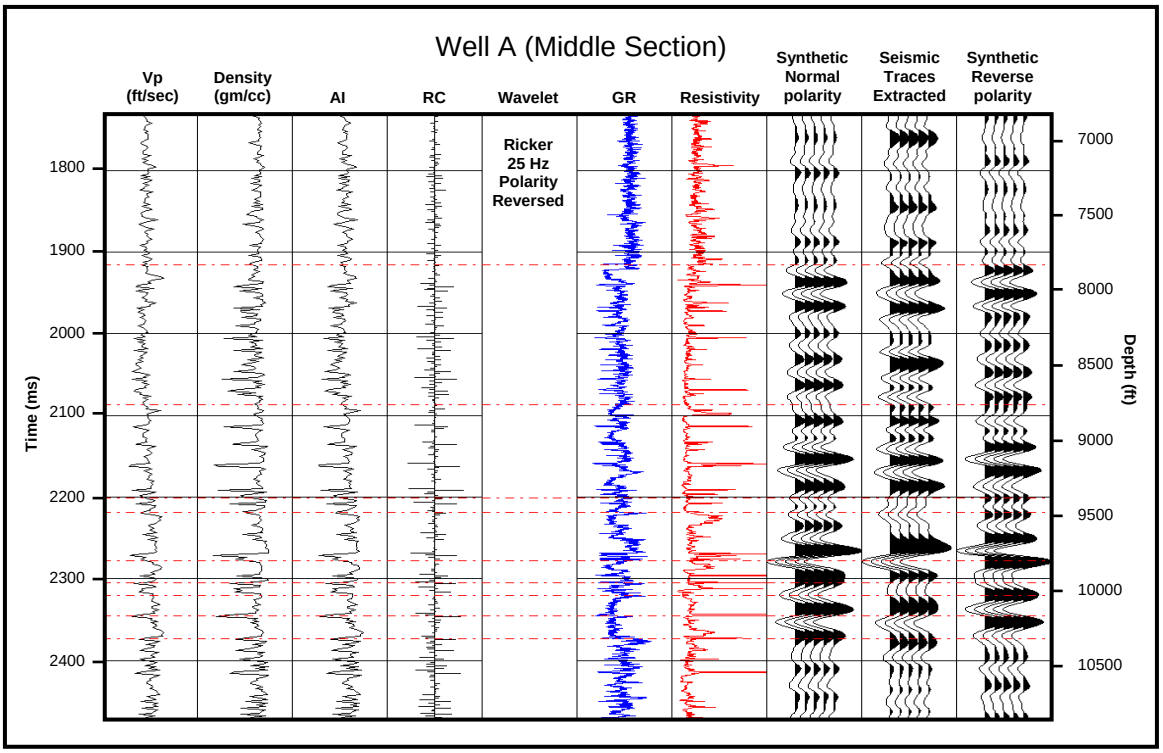

Figure A.2: Synthetic seismogram for the middle section of Well A using a Ricker wavelet of 25 Hz. The tie is good. A reverse polarity wavelet was used, demonstrating that the seismic needed a phase rotation of -180 degrees.

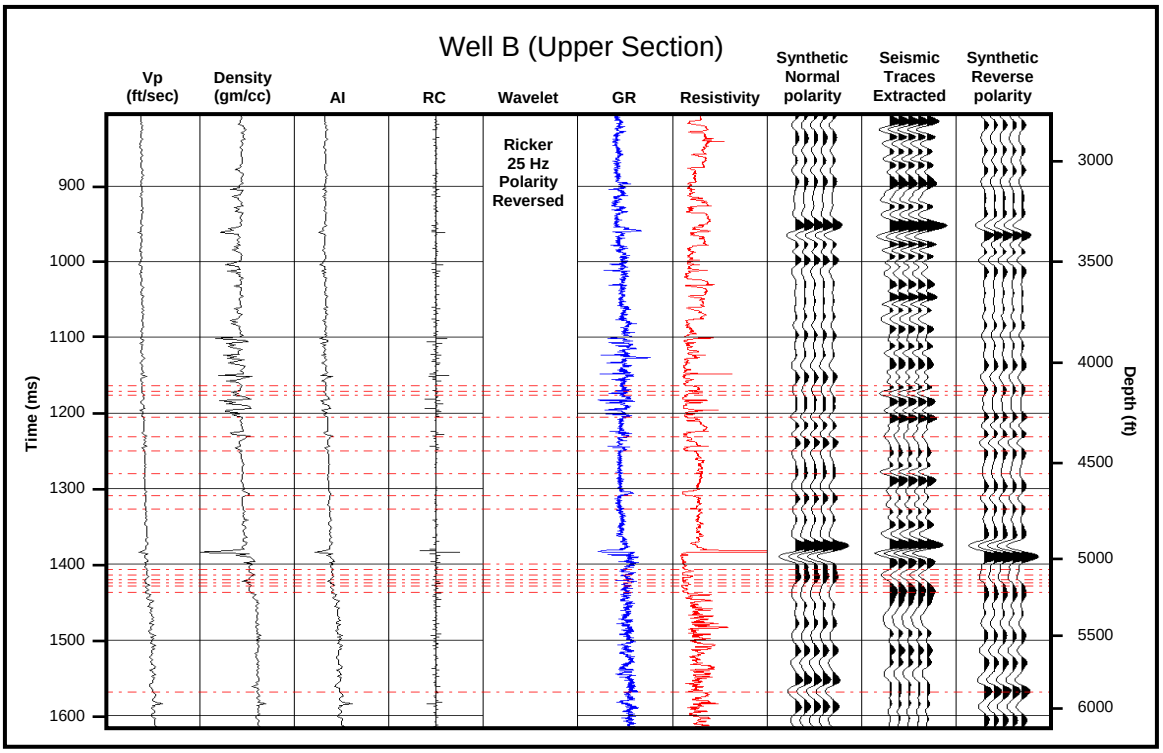

Figure A.3: Synthetic seismogram for the upper section of Well B using a Ricker wavelet of 25 Hz. The tie is fairly good. A reverse polarity wavelet was used, demonstrating that the seismic needed a phase rotation of -180 degrees.

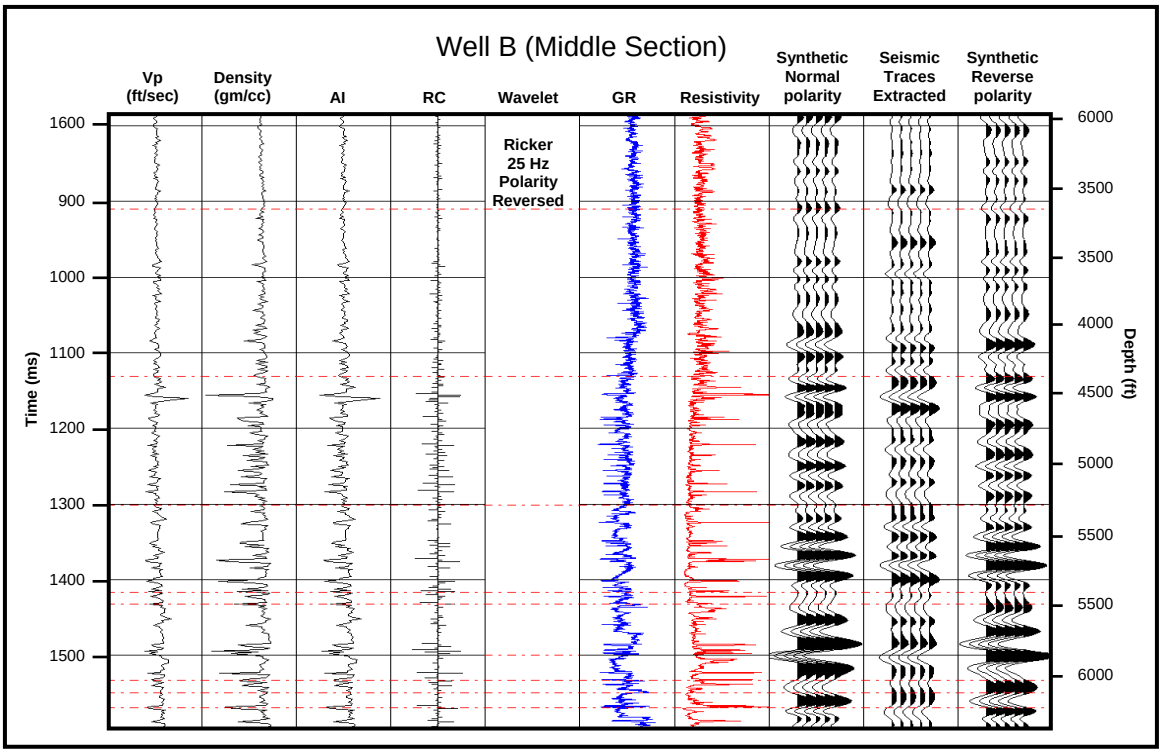

Figure A.4: Synthetic seismogram for the middle section of Well B using a Ricker wavelet of 25 Hz. The tie is fairly good. A reverse polarity wavelet was used, demonstrating that the seismic needed a phase rotation of -180 degrees.

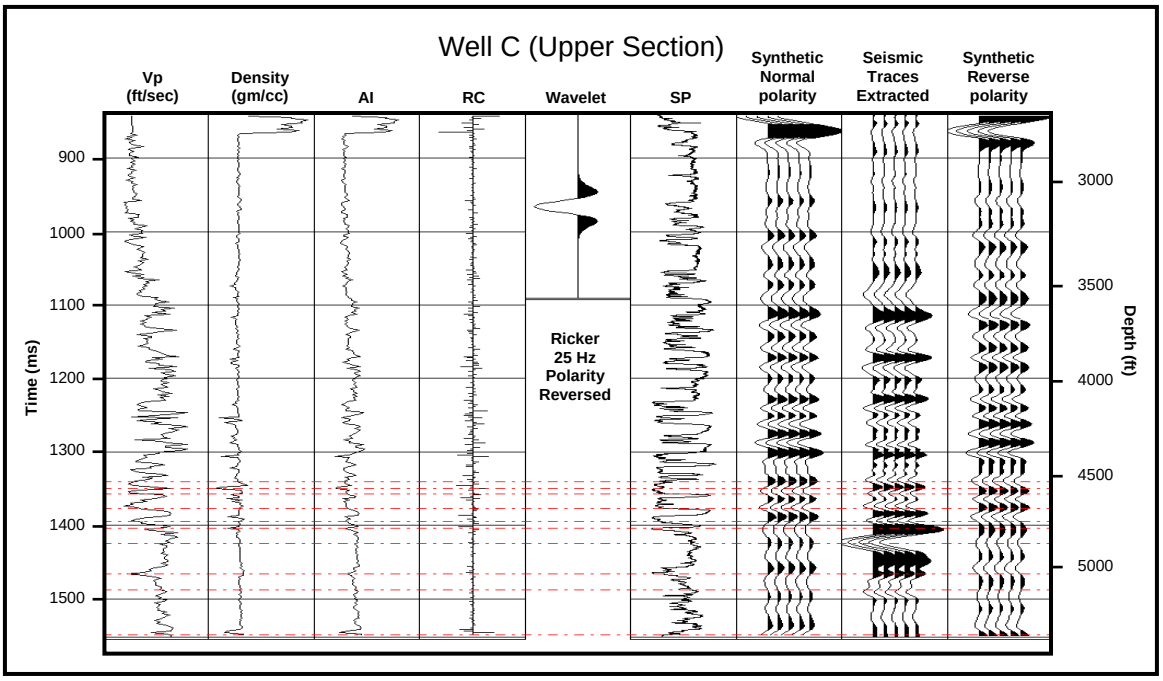

Figure A.5: Synthetic seismogram for the middle section of Well C using a Ricker wavelet of 25 Hz. The tie is fairly good. A reverse polarity wavelet was used, demonstrating that the seismic needed a phase rotation of -180 degrees.

APPENDIX B

Examples of the analysis of the wavelet-determination process using different wavelengths (240ms, 360 ms, 440 ms).

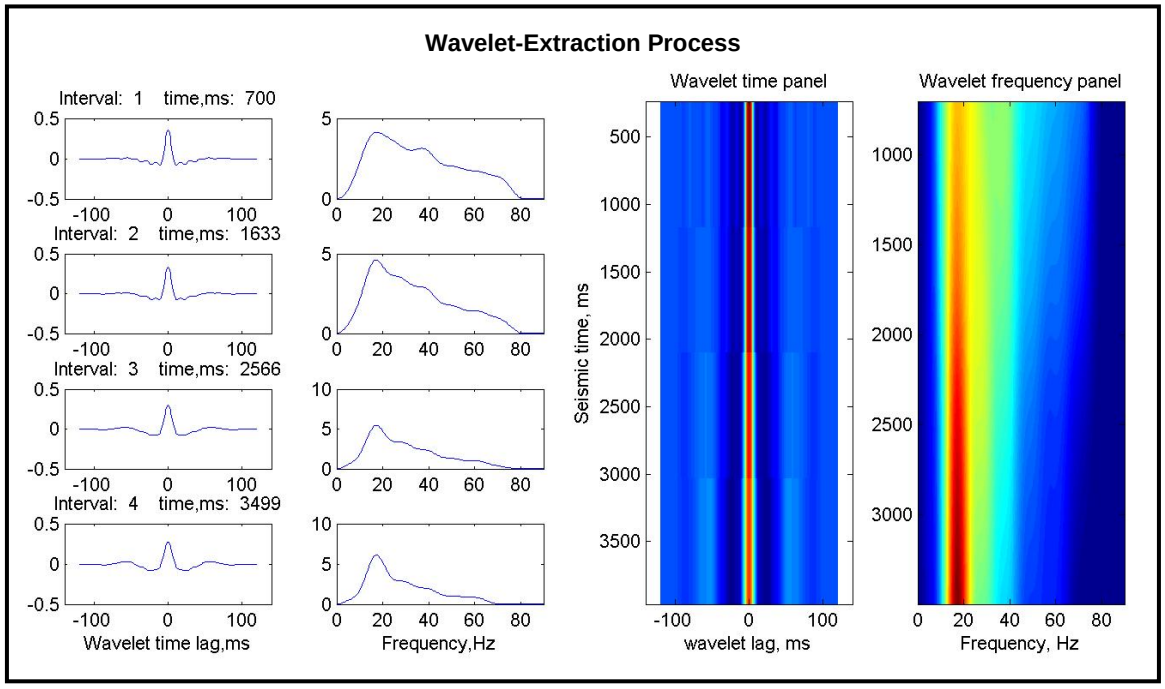

Figure B.1: Wavelet-extraction process showing the wavelet-amplitude spectrum variation as a function of time. The wavelength is 240 ms.

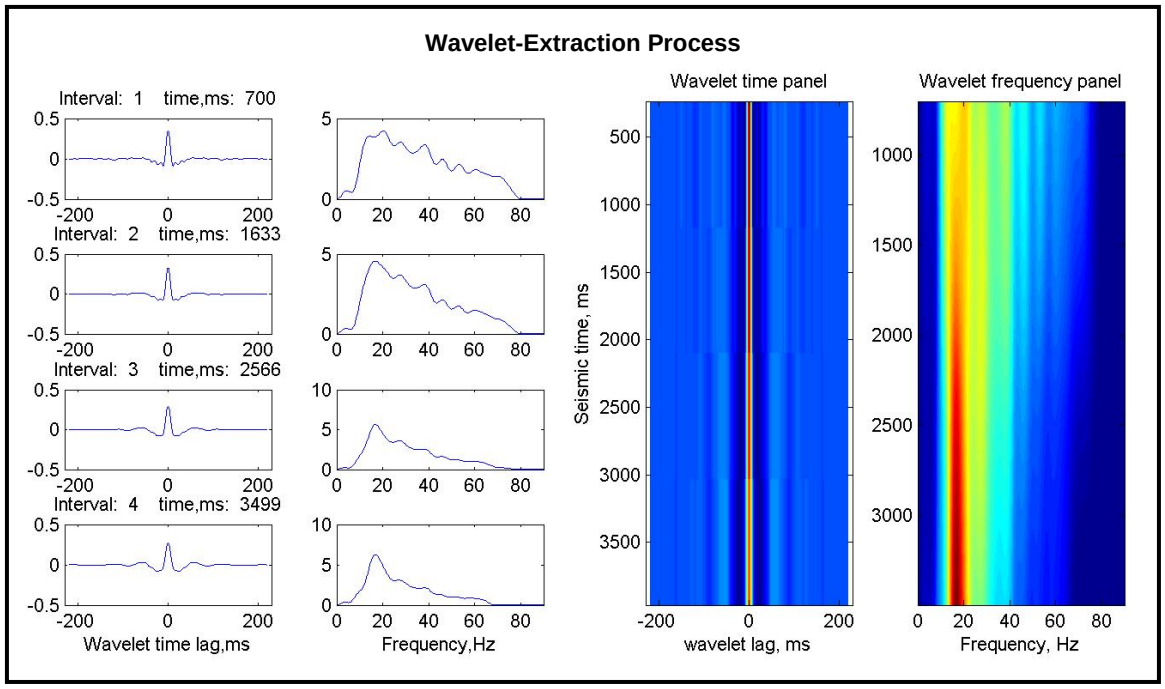

Figure B.2: Wavelet-extraction process showing the wavelet-amplitude spectrum variation as a function of time. The wavelength is 440 ms.

APPENDIX C

More spectral inversion results:

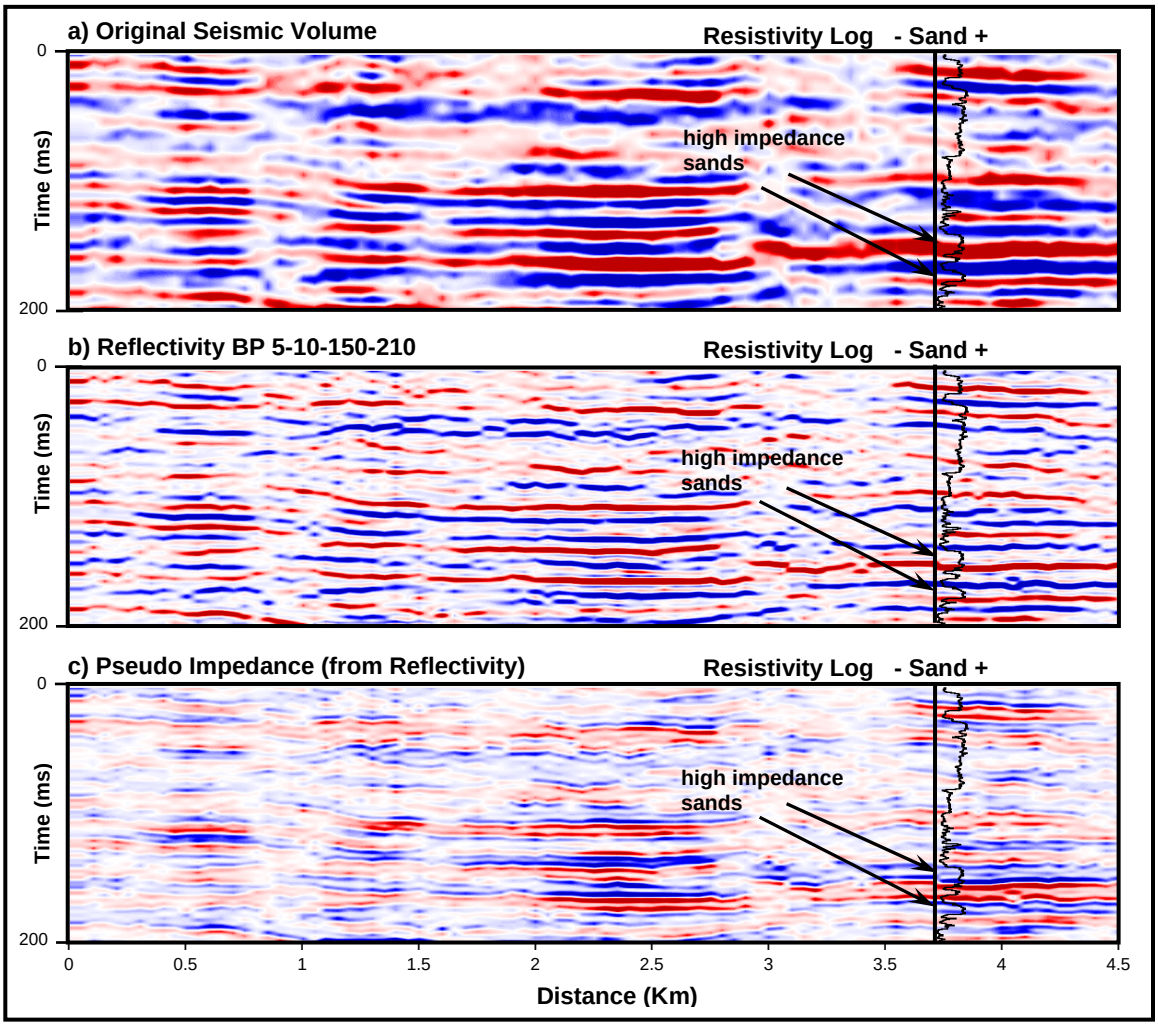

Figure C.1: Comparison of the original seismic (a), the reflectivity band limited 5-10-150-210 (b) and pseudo-impedance sections (c) with the induction well log. Two high impedance sands (13 and 7 ms time thickness respectively) are resolved by the inversion on the reflectivity and impedance volumes. The tuning thickness is 28 ms for the original seismic data. Both possible gas sands were located above the main reservoir and have not been proved yet.

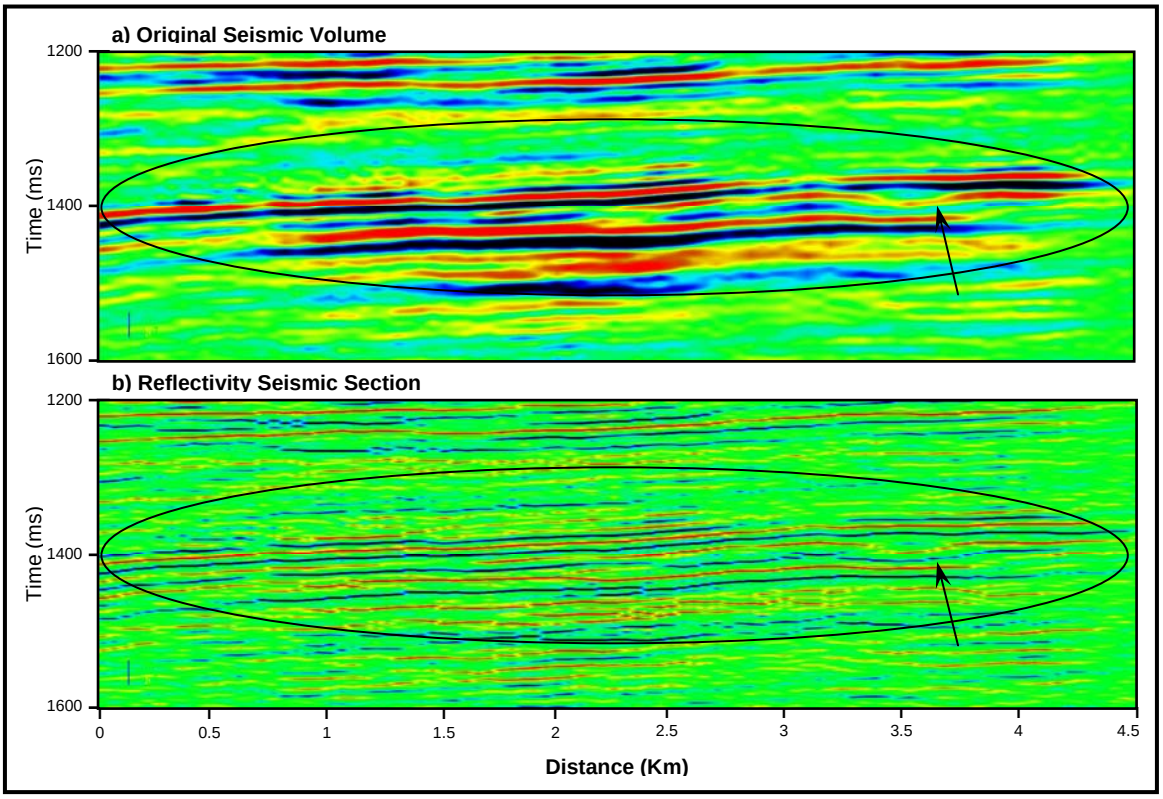

Figure C.2: Comparison between a full stack seismic (a) and the inverted sections (b). The vertical resolution and lateral continuity are significantly improved, especially within the elliptic area. The arrow shows what it could be part of a bar assemblage.

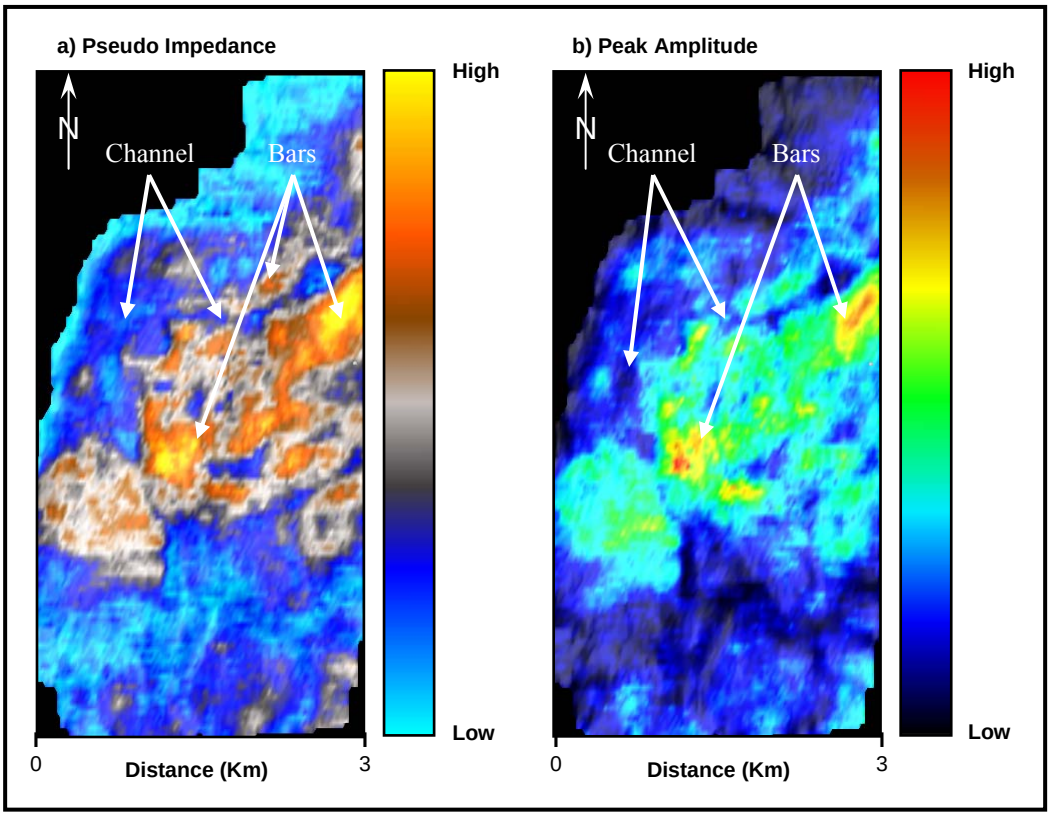

Figure C.3: Comparison between RMS amplitude extractions along the Sterling B2 horizon in a 20 ms time window for pseudo-impedance (a) and peak-amplitude (maximum amplitude value at every peak frequency) volumes (b). Notice some channel features or bars that could correspond with the analog case described of the Sagavanirktok River, northern Alaska.